Highly turbulent gas on GMC scales in NGC 3256, the nearest luminous infrared galaxy

Nathan Brunetti [iD],[1][*] Christine D. Wilson [iD],[1] Kazimierz Sliwa,[2] Eva Schinnerer,[2] Susanne Aalto[3] and Alison B. Peck[4]

[1]*Department of Physics and Astronomy, McMaster University, Hamilton, ON L8S 4M1, Canada*
[2]*Max-Planck-Institut für Astronomie, Königstuhl 17, D-69117 Heidelberg, Germany*
[3]*Department of Space, Earth and Environment, Chalmers University of Technology, Onsala Space Observatory, SE-43992 Onsala, Sweden*
[4]*Gemini Observatory, Northern Operation Center, 67-0 N. A'Ohoku Place, Hilo, HI, USA*

ABSTRACT

We present the highest resolution CO (2–1) observations obtained to date (0.25 arcsec) of NGC 3256 and use them to determine the detailed properties of the molecular interstellar medium in the central 6 kpc of this merger. Distributions of physical quantities are reported from pixel-by-pixel measurements at 55 and 120 pc scales and compared to disc galaxies observed by PHANGS-ALMA (Physics at High Angular resolution in Nearby GalaxieS with Atacama Large Millimeter/Submillimeter Array). Mass surface densities range from 8 to 5500 $M_\odot$ pc^{-2} and velocity dispersions from 10 to 200 km s^{-1}. Peak brightness temperatures as large as 37 K are measured, indicating the gas in NGC 3256 may be hotter than all regions in nearby disc galaxies measured by PHANGS-ALMA. Brightness temperatures even surpass those in the overlap region of NGC 4038/9 at the same scales. The majority of the gas appears unbound with median virial parameters of 7–19, although external pressure may bind some of the gas. High internal turbulent pressures of 10^5–10^{10} K cm^{-3} are found. Given the lack of significant trends in surface density, brightness temperature, and velocity dispersion with physical scale we argue the molecular gas is made up of a smooth medium down to 55 pc scales, unlike the more structured medium found in the PHANGS-ALMA disc galaxies.

Key words: ISM: clouds – ISM: jets and outflows – ISM: kinematics and dynamics – galaxies: interactions – galaxies: ISM – galaxies: jets.

1 INTRODUCTION

Molecular gas is the immediate fuel for star formation and thus an important ingredient in galaxy evolution. In the Milky Way and nearby galaxies, giant molecular clouds (GMCs) are the dominant structures within the molecular interstellar medium (ISM, Dame et al. 1987; Solomon et al. 1987; Wilson & Scoville 1990; Fukui et al. 1999; Mizuno et al. 2001; Engargiola et al. 2003; Leroy et al. 2006; Rosolowsky 2007) and are the sites of current and future star formation (Blitz & Thaddeus 1980; Genzel & Stutzki 1989; Mizuno et al. 1995). However, different galactic environments exhibit molecular gas properties that vary widely while also maintaining ongoing star formation (e.g. Rosolowsky & Blitz 2005; Heyer et al. 2009; Wong et al. 2011; Leroy et al. 2015). A complete description of the evolution of molecular gas properties and their connections to star formation must include explanations spanning the full range of observed regimes.

Wide distributions of molecular gas mass surface densities and velocity dispersions have been observed in many regions within the Milky Way and nearby galaxies (e.g. Heyer, Carpenter & Snell 2001; Heyer et al. 2009; Wong et al. 2011; Bolatto et al. 2008; Colombo et al. 2014; Rosolowsky & Blitz 2005; Leroy et al. 2015; Utomo et al. 2015; Sun et al. 2018). The largest and most uniform extragalactic

sample was analysed by Sun et al. (2018) including 11 galaxies in the Physics at High Angular resolution in Nearby GalaxieS with Atacama Large Millimeter/Submillimeter Array (PHANGS-ALMA) survey (Leroy et al., in preparation), along with four galaxies from the literature. They found these properties vary systematically such that a narrow range of virial parameters (∼1 to 3) is present. As an estimate of the balance between the kinetic energy, K, and gravitational energy, U_g, within a molecular cloud, the virial parameter, $\alpha_{vir} \equiv 2K/U_g$, can indicate the likelihood of collapse and the ability to form stars (McKee & Zweibel 1992; Federrath & Klessen 2012; Krumholz, Dekel & McKee 2012; Padoan et al. 2017). These galaxies were also found to exhibit internal turbulent pressures ranging across 4–5 orders of magnitude. The internal pressure, $P_{turb} \propto \sigma^2/R$, can be estimated from observational properties of clouds and comparing the pressure to the surface density of the cloud can provide another estimate its dynamical state (Keto & Myers 1986; Heyer et al. 2009; Field, Blackman & Keto 2011; Leroy et al. 2015). These results imply the majority of molecular gas is kept close to dynamical equilibrium or collapse while the internal energy varies dramatically. Combining those molecular gas observations with measurements of the atomic and stellar surface densities, Sun et al. (2020a) estimated the external pressure exerted on GMCs. They found that maintaining dynamical equilibrium over such a large range of internal pressures requires taking into account the full external pressure exerted on GMCs from the atomic, stellar, and clumpy molecular components of the galaxy.

[*] E-mail: brunettn@mcmaster.ca

While the PHANGS-ALMA analyses cover a range of galactic environments, they lack a direct comparison with observations of more extreme systems that bracket their sample. Do the scalings found by Sun et al. (2018) hold as gas masses, gas densities, and star formation rates (SFRs) continue to climb? For example, star formation efficiencies per freefall time within ultra/luminous infrared galaxy (U/LIRGs) have been estimated to be higher than in disc galaxies. Calculated on scales of ~500 pc in five U/LIRGs, Wilson et al. (2019) find efficiencies per freefall time ~5 to 10 times higher than those found by Utomo et al. (2018) for disc galaxies between 60 to 120 pc. To effect a change in the rate at which molecular gas is converted to stars, there is likely a change in the structure and dynamics of the molecular gas from which the stars form. In this work, we concentrate on the starburst regime for studying these questions.

Many U/LIRGs are gas-rich major mergers where the structure of the ISM is strongly influenced by galaxy-scale dynamics (Sanders & Mirabel 1996; Farrah et al. 2001; Veilleux, Kim & Sanders 2002). Tidal torques on the gas lead to bulk gas inflow towards the centres of mergers (e.g. Noguchi 1988; Mihos & Hernquist 1996; Iono, Yun & Mihos 2004). These gas motions can enhance star formation by adding additional external pressure on to GMCs, or they could suppress star formation through the release of gravitational potential energy injecting turbulent energy into the molecular gas (Krumholz et al. 2018). Enhanced star formation is observed in merger systems which means that the ISM is also subjected to large amounts of clustered stellar, supernova, and cosmic ray-heating feedback which can dramatically shape the ISM and subsequent star formation (Dale & Bonnell 2008; Klassen, Pudritz & Peters 2012; Howard, Pudritz & Harris 2017; Keller, Kruijssen & Wadsley 2020; Booth et al. 2013; Girichidis et al. 2016). The stellar activity can also pump turbulent energy into the molecular gas. The exact balance of these competing processes is not well constrained, nor is their coupling to GMC scales in these highly active systems.

Very high angular resolution observations are required to resolve GMC sizes of 50–100 pc in these distant systems. As the nearest LIRG, NGC 3256 is a prime target to explore these effects on molecular gas in a merger for comparison with nearby disc galaxies. At a distance of 44 Mpc (CMB-corrected redshift from NED adopting *WMAP* five-year cosmology of $H_0 = 70.5\,\mathrm{km\,s^{-1}\,Mpc^{-1}}$, $\Omega = 1$, and $\Omega_\mathrm{m} = 0.27$), the ALMA can readily resolve molecular gas on the scale of GMCs. Its infrared (IR) luminosity is $L_{8-1000\,\mathrm{\mu m}} \sim 4 \times 10^{11}\,\mathrm{L_\odot}$ (Sanders et al. 2003) and total SFR is ~50 $\mathrm{M_\odot\,yr^{-1}}$ (Sakamoto et al. 2014). It is a late-stage merger (Stierwalt et al. 2013) with two distinguishable nuclei separated by ~1.1 kpc (Sakamoto et al. 2014, adjusted to our assumed distance of 44 Mpc) that share a common envelope. The relatively face-on northern nucleus is producing a molecular outflow aimed roughly along the line of sight (see diagrams in Sakamoto et al. 2014; Harada et al. 2018), which is powered by the starburst (Sakamoto et al. 2014). The southern nucleus is nearly edge-on with an extremely collimated jet being launched in the north–south direction. Calculations by Sakamoto et al. (2014) found that the energy budget for the southern jet likely has a contribution from a highly obscured active galactic nucleus (AGN). This is consistent with IR and X-ray observations by Ohyama, Terashima & Sakamoto (2015) indicating an AGN in the southern nucleus. Modelling of resolved multiline and multitransition molecular observations by Michiyama et al. (2018) also suggest the southern outflow may contain two phases produced by the interaction of the jet with the ISM.

In this paper, we present the highest resolution carbon monoxide (CO) observations obtained to date of NGC 3256 and use them to study the detailed properties of the molecular ISM. Section 2 summarizes our observations and imaging procedure. Section 3 describes the steps used in analysing NGC 3256 to reproduce the methods used by Sun et al. (2018). In Section 4, we compare physical quantities such as surface density, velocity dispersion, peak brightness temperature, virial parameter, and turbulent pressure to those from the preliminary PHANGS-ALMA sample reported by Sun et al. (2018). We discuss the implications for the structure of the ISM in NGC 3256 in Section 5. Section 6 summarizes the conclusions and future work.

2 DATA

2.1 Observations

Spectral line and continuum observations were carried out with the 12 m main array, the 7 m Atacama Compact Array (ACA), and the total power (TP) antennas recovering all spatial scales down to ~0.25 arcsec. Two separate configurations of the 12 m array were used. Table 1 briefly summarizes the observations.

The J=2–1 rotational transition of CO and J=5–4 transition of carbon monosulfide (CS) were each targeted with two overlapping spectral windows (SPWs). This was done to ensure the spectral line wings from the nuclear outflow and jet would be captured. Enough line-free channels were available to produce a continuum map as well.

2.2 Calibration

Calibration was carried out at the observatory and we produced our own cubes. Common Astronomy Software Applications (CASA) was used for both calibration and imaging (McMullin et al. 2007). Software versions used are summarized in Table 1.

We inspected the calibration quality by plotting amplitudes and phases versus frequency, time, and *uv* distance for all calibrator sources. We found that flagging the two antennas with the greatest separations from the array centre improved the synthesized beam pattern and root-mean-square (rms) noise. Significant continuum emission is detected in all interferometric SPWs at the positions of the two nuclei so we performed continuum subtraction, fitting with a zeroth-order polynomial in the frequency ranges 226.599–27.427, 229.134–229.497, and 229.759–230.208 GHz.

Due to the complexity of combining observations from so many different dates, configurations, and arrays we found that performing all gridding and SPW combination with the *mstransform* task, before producing cubes, gave the best results. Our criteria for quality in this step were small rms noise variations from channel to channel and minimal discontinuities in the resultant spectra when transitioning from one SPW to the other.

Dirty CO cubes were produced from the calibrated and continuum-subtracted *uv* data using the *tclean* task in CASA version 5.4.0-68. Channels were gridded to 3.906 MHz width (about 5.131 km s^{-1}), starting at 2004 km s^{-1} and ending at 3599 km s^{-1}.

The TP data were calibrated and imaged with the ALMA single dish pipeline. The baseline subtraction step was modified to handle the fact that the CO line emission extended to one end of each SPW. Despite the modified baseline fitting, there still existed a difference of up to ~9 per cent between the line intensities between the two CO SPWs. We tested the total flux measurement by manually stitching together the two TP SPWs and making an integrated intensity map from this cube. We found at least ~83 per cent of the flux was recovered in the interferometric observations using the combined 12 and 7 m data. Given the uncertainties in the baseline subtraction process, we chose not to incorporate the TP observations into imaging the interferometric data to avoid introducing artifacts.

Table 1. Summary of observations and calibration methods.

Array	Observation date	Repeats	Minimum baseline[a] (m)	Maximum baseline[a] (m)	Calibration type	CASA version
12 m	2016 September 1	1	12	1713	Pipeline	4.7.0 r38335; PL 38366 Cycle4-R2-B
12 m	2016 September 7	1	14	2861	Pipeline	4.7.0 r38335; PL 38366 Cycle4-R2-B
12 m	2016 March 10	1	13	429	Manual	4.6.0 r36590
7 m	2015 November 2	1	9	44	Manual	4.5.1 r35996
7 m	2015 November 5	2	8	43	Manual	4.5.1 r35996
7 m	2015 November 6	2	7	44	Manual	4.5.1 r35996
7 m	2015 November 7	2	8	43	Manual	4.5.1 r35996
7 m	2015 December 15	2	7	43	Manual	4.5.1 r35996
TP	2015 December 5	4	...	...	Pipeline	4.5.2 r36115; PL 36252 Cycle3-R4-B
TP	2015 December 6	2	...	...	Pipeline	4.5.2 r36115; PL 36252 Cycle3-R4-B
TP	2015 December 15	6	...	...	Pipeline	4.5.2 r36115; PL 36252 Cycle3-R4-B
TP	2016 March 5	1	...	...	Pipeline	4.5.2 r36115; PL 36252 Cycle3-R4-B

Notes: All interferometric observations were multiple-pointing mosaics covering an area with a radius approximately 30 arcsec centred on RA: $10^h27^m51^s$ Dec.: $-43°54'15''$. SPWs were centred at 227.526, 229.284, 241.790, and 243.547 GHz. Each had a bandwidth of 1.875 GHz and native spectral resolution of 1.953 MHz.

[a] Projected for source position on the sky.

2.3 Imaging CO

To help guide the clean algorithm in modelling emission on both scales larger than the synthesized beam and point sources, we ran multiscale and point-source cleaning in two separate passes. The first pass was a shallow multiscale clean using very extended hand-drawn clean masks and excluding point-source models. The second pass continued cleaning but this time using only point-source models. New masks were produced in the second pass because only compact emission remained and new masks were made to closely follow those features. Masking was accomplished primarily with the automultithresh algorithm, but we also manually edited the masks at each major cycle.

3 ANALYSIS

Following Sun et al. (2018), we convolved the dirty and cleaned CO cubes to have circular synthesized beams with full width at half-maximum (FWHMs) of 55, 80, and 120 pc. Pixels in the convolved cubes were resampled to a coarser grid of square pixels that were FWHM/2 on a side, thus Nyquist sampling the beams.

To derive physical properties of the molecular gas traced by the CO observations we calculated moment 0 (integrated intensity) and 2 (intensity-weighted velocity dispersion) maps. Signal masks for moment map calculations were produced following the procedure[1] used by Sun et al. (2018, hereafter referred to as the Sun thresholding), and we refer the reader to their description of the algorithm outlined in their section 3.2. These signal masks were then used in producing moment maps with the standard functions in the SPECTRAL-CUBE library (Ginsburg et al. 2019). The Sun thresholding appeared superior to standard n–σ thresholding due to its conservative treatment of the outer regions of our field of view (FoV), its ability to extract low signal-to-noise (S/N) emission without introducing significant numbers of noisy pixels, and being the only method that made the northern outflow clearly visible in the moment 2 map.

[1] The PYTHON script for producing the signal masks were obtained from https://github.com/astrojysun/Sun_Astro_Tools/blob/master/sun_astro_tools/spectralcube.py.

To convert the integrated intensity maps to mass surface density units, we adopt the U/LIRG CO-to-H$_2$ conversion factor (Downes & Solomon 1998), including a factor of 1.36 to account for helium. Following the procedure of He et al. (2020) to determine the appropriate conversion factor we use the stellar mass of NGC 3256 from Howell et al. (2010) of 1.14×10^{11} M$_\odot$ and estimate the expected specific star formation rate (sSFR) using the xGASS (extended GALEX Arecibo SDSS Survey) star-forming main-sequence fit log sSFR$_{MS}$ = $-0.344(\log M_\star - 9) - 9.822$ from Catinella et al. (2018). Using the $M_\star$ and SFR, we calculate the ratio of the actual sSFR to the main sequence expected sSFR to be 15. This ratio puts NGC 3256 well away from the star-forming main-sequence locus indicating a probability near 100 per cent of NGC 3256 being in a starburst phase (Sargent et al. 2014). The conversion factor recipe from Violino et al. (2018) is $\alpha_{CO} = (1 - f_{SB}) \times \alpha_{CO, MS} + f_{SB} \times \alpha_{CO, SB}$, where f_{SB} is the probability of a galaxy being in a starburst phase. $\alpha_{CO, MS}$ and $\alpha_{CO, SB}$ are the main sequence and starburst conversion factors expected in the 2-Star Formation Mode framework of Sargent et al. (2014). Using this recipe, we estimate that the conversion factor would be dominated by the starburst value so we adopt it for simplicity.

We adopt the mean ratio CO J=2–1/1–0 = 0.79 from the xCOLD GASS sample (extended CO Legacy Database for GASS; Saintonge et al. 2017) which is consistent with the ratio of 0.8 ± 0.22 measured in NGC 3256 by Aalto et al. (1995) in a single-dish beam roughly the size of our FoV. This ratio results in a conversion factor from the integrated 2–1 line to molecular gas mass of α_{CO} = 1.38 M$_\odot$ pc^{-2}(K km s^{-1})$^{-1}$. The 2–1 / 1–0 ratio may be larger in U/LIRGs (Papadopoulos et al. 2012; Saito et al. 2017; He et al. 2020) than the normal spirals studied by xCOLD GASS, which would result in the surface densities presented here overestimating the true surface densities. It is also likely there is considerable variation in the line ratio within NGC 3256 (Harada et al., in preparation).

As in Sun et al. (2018), we corrected the velocity dispersion estimates measured in the moment 2 maps for the finite channel widths using equations (15)–(17) from Leroy et al. (2016). To measure the correlation between channels we calculated the Pearson correlation coefficient between each channel ('x-value') and the next channel ('y-value'). The correction is always less than 1 km s^{-1} but we chose to apply it to all of our measured velocity dispersions to replicate the procedure of Sun et al. (2018).
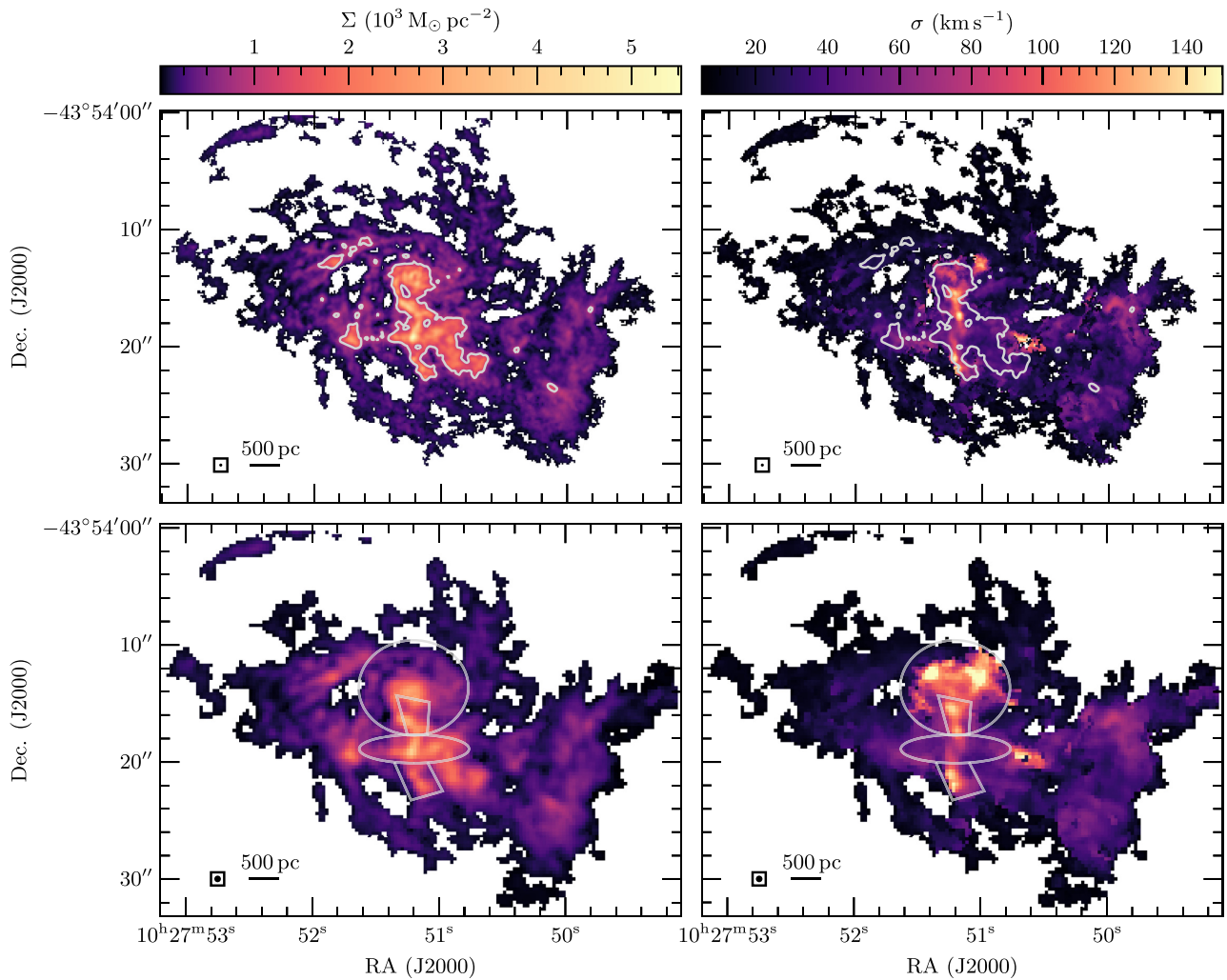
Figure 1. Maps of molecular gas mass surface density (left) and velocity dispersion (right), with a synthesized beam FWHM of 55 pc (top) and 120 pc (bottom). Contours in the top row are at a surface density of $1000 \, M_\odot \, pc^{-2}$. The same contours are in the left- and right-hand frames. Grey ellipses in the bottom row mark the central 1 kpc, projected to account for the inclination angles of the nuclei. Grey polygons indicate pixels affected by the southern jet, identified in the dispersion maps, that are not included in the distributions of measured quantities shown in subsequent figures. Pixels west of an RA of approximately $10^h 27^m 50.3^s$ are also excluded from our distribution analyses due to complex spectral features and potential interferometric-sidelobe contamination. The beam sizes are represented by the black circles in the bottom-left corners of each frame. The U/LIRG conversion factor of $1.38 \, M_\odot \, pc^{-2} (K \, km \, s^{-1})^{-1}$ was used to convert the integrated intensity maps from $K \, km \, s^{-1}$ to $M_\odot \, pc^{-2}$. Multiplying the surface densities by ~ 4.5 would convert to the Galactic conversion factor of $6.25 \, M_\odot \, pc^{-2} (K \, km \, s^{-1})^{-1}$. Both of these conversion factors include a factor of 1.36 to account for helium.

Fig. 1 shows mass surface density and velocity dispersion maps of NGC 3256, convolved to synthesized beam sizes of 55 and 120 pc. Grey contours at the $1000 \, M_\odot \, pc^{-2}$ level are shown in the top row. The bottom row includes grey ellipses marking the inclination-projected central 1 kpc radii, centred on the positions of the nuclei, and grey polygons marking pixels heavily contaminated by the southern jet, identified in the velocity dispersion maps.

The FoV shown is centred at RA $10^h 27^m 51^s$ (Dec.) $-43°54'16''$, and it covers 0.73 arcmin in RA and 0.54 arcmin in Dec. Pixels west of an R.A. of approximately $10^h 27^m 50.3^s$ are excluded from our analysis. In this region, there are elevated velocity dispersions measured coming from two-component spectral profiles. While multicomponent lines near the centre of the system appear to be produced by multiple gas components along the line of sight, we believe some of the two-component profiles in the west are the result of imperfectly cleaned sidelobes of the interferometric synthetic

beam. It also appears material from the outskirts of the progenitors are overlapping along the line of sight (Sakamoto et al. 2014), producing spectral profiles that are too complex for the moment-based analysis here. For this reason, we exclude pixels from that part of the maps from the measurements we present.

4 RESULTS

In this section, we present mass-weighted Gaussian kernel density estimator (KDE) distributions of the mass surface densities, velocity dispersions, peak brightness temperatures, virial parameters, and internal turbulent pressures in NGC 3256. The distributions measured in the PHANGS-ALMA early sample from Sun et al. (2018) are also shown for comparison. Virial parameters and turbulent pressures are calculated in the same way as by Sun et al. (2018) and assuming the diameter of the cloud is equal to the beam FWHM.

Table 2. Mass-weighted percentiles of all measured and derived quantities from NGC 3256, by region and resolution.

Region	Beam Size (pc)	Σ (M$_\odot$ pc^{-2})			σ (km s^{-1})			$T_{\rm peak}$ (K)			$\alpha_{\rm vir}$			$P_{\rm turb}$ (10^6 K cm^{-3})		
		16	50	84	16	50	84	16	50	84	16	50	84	16	50	84
Non-nuclear	55	150	390	1300	12	25	43	2.7	5.1	11	5.5	11	26	2.3	26	170
	80	150	380	1200	13	27	45	2.4	4.6	10	4.3	8.8	20	1.8	20	120
	120	140	370	1200	14	28	47	2.2	4.2	9.5	3.4	6.8	15	1.3	15	92
Nuclei	55	520	1400	2500	27	46	71	5.8	12	19	6.1	13	28	36	270	930
Combined	80	520	1400	2500	34	55	89	5.4	11	17	5.6	13	29	48	250	970
	120	500	1500	2400	45	66	100	5.1	9.9	16	5.2	12	34	75	210	720
Northern	55	410	870	2400	20	42	72	5.1	11	20	6.2	13	29	18	160	820
Nucleus	80	410	870	2300	25	62	95	4.8	9.7	19	6.7	18	40	18	280	1000
	120	390	850	2200	44	85	110	4.4	8.6	15	7.4	19	63	30	260	800
Southern	55	970	1700	2800	36	49	70	6.5	13	18	5.9	12	24	160	330	1200
Nucleus	80	980	1700	2600	39	51	73	6.3	12	17	4.7	9.7	19	130	250	940
	120	1100	1700	2500	45	54	76	6.4	12	16	4.1	7.6	13	98	190	620

Distributions include measurements from all pixels containing significant emission and smoothed to 55 and 20 pc. We also calculated distributions for 80 pc but do not show them because they always land mid-way between the distributions from 55 and 120 pc. A bandwidth of 0.1 dex was used for all distributions except the internal turbulent pressure where a bandwidth of 0.2 dex was used instead. This matches the KDE calculations of Sun et al. (2018) where the bandwidth for their pressures was misreported as 0.1 dex (Sun, private communication).

In the following plots, distributions of pixels from the entire mapped FoV are shown as solid lines, pixels within a radius of 1 kpc from the nuclei as dotted lines, and pixels outside the central 1 kpc radius as dashed lines (referred to here as the non-nuclear pixels and equivalent to the disc pixels in Sun et al. 2018). The nuclear peaks in our continuum map were used as the positions of the nuclei.

We then projected the boundaries of the central kiloparsec circles to account for the inclination angles of 30° for the northern nucleus (Sakamoto et al. 2014) and 75° for the southern nucleus. Although Sakamoto et al. (2014) estimate an inclination angle of 80° for the southern nucleus, we adopt 75° because it better captures the apparent thickness of the southern disc in these data. However, the difference is small as an inclination of 75° results in about 8 pixels across the minor axis in the 120 pc maps, while 80° would result in 5 pixels. The grey ellipses in the bottom row of Fig. 1 show these central region boundaries. We do not correct the measurements for these inclinations because the disturbed morphology makes it unclear where the boundaries of the inclination regions should be or how to transition between them. There is also the complication of how to deal with overlapping material from the two nuclei. Not including inclination corrections will cause our surface density measurements to overestimate the true values perpendicular to any discs present.

Grey polygons indicate pixels associated with the southern jet and those pixels are excluded from all distributions and total masses used to normalize the KDEs. Table 2 presents the 16th, 50th, and 84th percentiles for the different regions of NGC 3256, at each resolution. Comparisons of these percentiles for NGC 3256 and the PHANGS-ALMA sample at 120 pc resolution are presented in Figs 2–6.

4.1 Mass surface density

At all resolutions, NGC 3256 exhibits surface density distributions with a maximum centred near 2000 M$_\odot$ pc^{-2} and a shoulder centred near 600 M$_\odot$ pc^{-2} (see Fig. 2). We measure that at least 85 per cent of the area out to 2 kpc from the mid-point between the two nuclei has $\Sigma \gtrsim 100$ M$_\odot$ pc^{-2}, independent of resolution.

The mass in the higher surface density peak of the distribution is dominated by pixels in the nuclear regions, but there is a significant contribution from pixels outside the central kiloparsec as well. Contours in the top row of Fig. 1 show the pixels with $\Sigma > 1000$ M$_\odot$ pc^{-2}. The majority of these pixels lie in the nuclear and southern jet regions, though not all nuclear pixels are at these high surface densities.

The lower surface density shoulder of the pixel distribution is a roughly equal mix of nuclear and non-nuclear pixels, but switches to being dominated by the non-nuclear pixels around 600 M$_\odot$ pc^{-2}. The central high density region is better described in the northern nucleus of NGC 3256 by a radius of 250 pc than the 1 kpc used for the PHANGS-ALMA galaxies. Considering the extra-nuclear high surface density lines of sight and low surface density pixels within the central kiloparsec, a careful decomposition of the gas emission using spatial and spectral dimensions will be crucial to fully understand the complex morphology of this merger. The pixel distributions throughout this section provide bulk measurements of the gas properties, but evaluation of those properties ultimately needs to be done on a sightline-by-sightline basis.

Comparing the mass surface densities measured in NGC 3256 to PHANGS-ALMA in the bottom row of Fig. 2, NGC 3256 occupies the high end of the distributions observed in the PHANGS-ALMA sample. The nuclei of most PHANGS-ALMA galaxies are consistent with the nuclei and upper range of the non-nuclear distribution in NGC 3256. Most disc distributions from PHANGS-ALMA overlap with the lower half of the non-nuclear distribution in NGC 3256.

4.2 Velocity dispersion

Velocity dispersions in NGC 3256 from all pixels and resolutions show a broad distribution in Fig. 3, ranging from 10 to 200 km s^{-1} and with a single peak near 50 km s^{-1}. The distribution does broaden towards higher dispersions going from 55 to 120 pc resolution. The non-nuclear distribution peaks near 30 km s^{-1} (independent of resolution), and the nuclear distribution peak increases from near 50 km s^{-1} at 55 pc to 70 km s^{-1} at 120 pc. Separating the nuclei in Table 2 shows that while both nuclei shift to higher dispersions at lower resolution, the northern nucleus has a much stronger trend with reso-
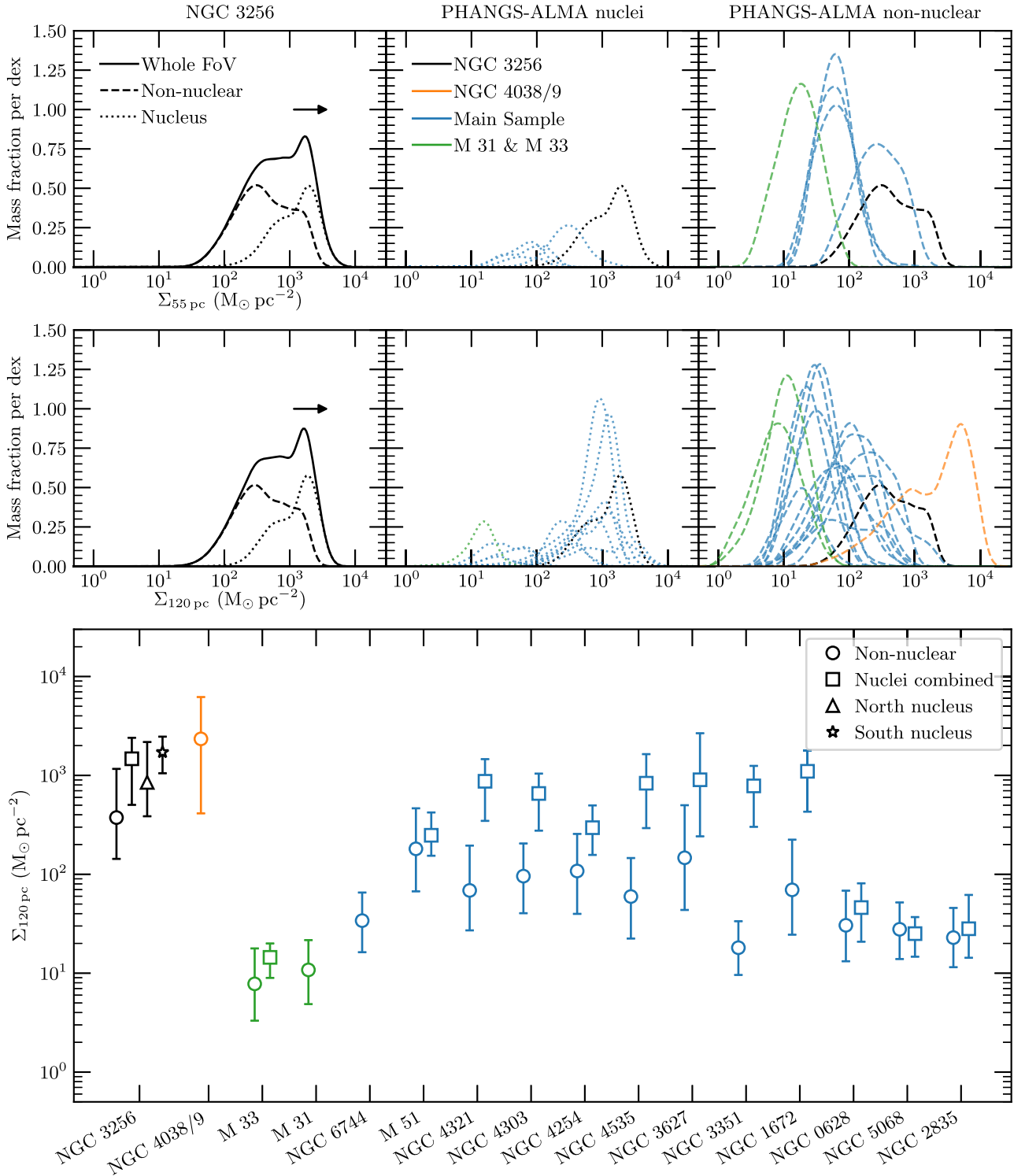
Figure 2. Molecular gas mass surface densities measured in NGC 3256 and the Sun et al. (2018) PHANGS-ALMA sample. Measurements for NGC 3256 are made in maps with beam FWHM of 55 and 20 pc and pixels half those lengths on a side. PHANGS-ALMA distributions come from maps with beam FWHM of 45 and 120 pc and pixels half those lengths on a side. Top and middle rows: solid lines are pixel distributions from the entire FoV, dashed lines are non-nuclear region pixels, and dotted lines are nuclear region pixels. Arrows show how values would shift if we adopt the Milky Way CO conversion factor of $6.25\,M_\odot\,\mathrm{pc}^{-2}(\mathrm{K\,km\,s}^{-1})^{-1}$ (used for all PHANGS-ALMA galaxies) instead of the LIRG conversion factor of $1.38\,M_\odot\,\mathrm{pc}^{-2}(\mathrm{K\,km\,s}^{-1})^{-1}$. PHANGS-ALMA galaxies are separated into nuclear and disc regions in the centre and right-hand panels, respectively, with the corresponding curves from NGC 3256 reproduced from the left panels. Bottom row: mass-weighted medians shown as symbols and ranges encompassing the inner 68 per cent of the distributions shown as error bars for NGC 3256 and the Sun et al. (2018) sample. All percentiles are calculated from the 120 pc maps.
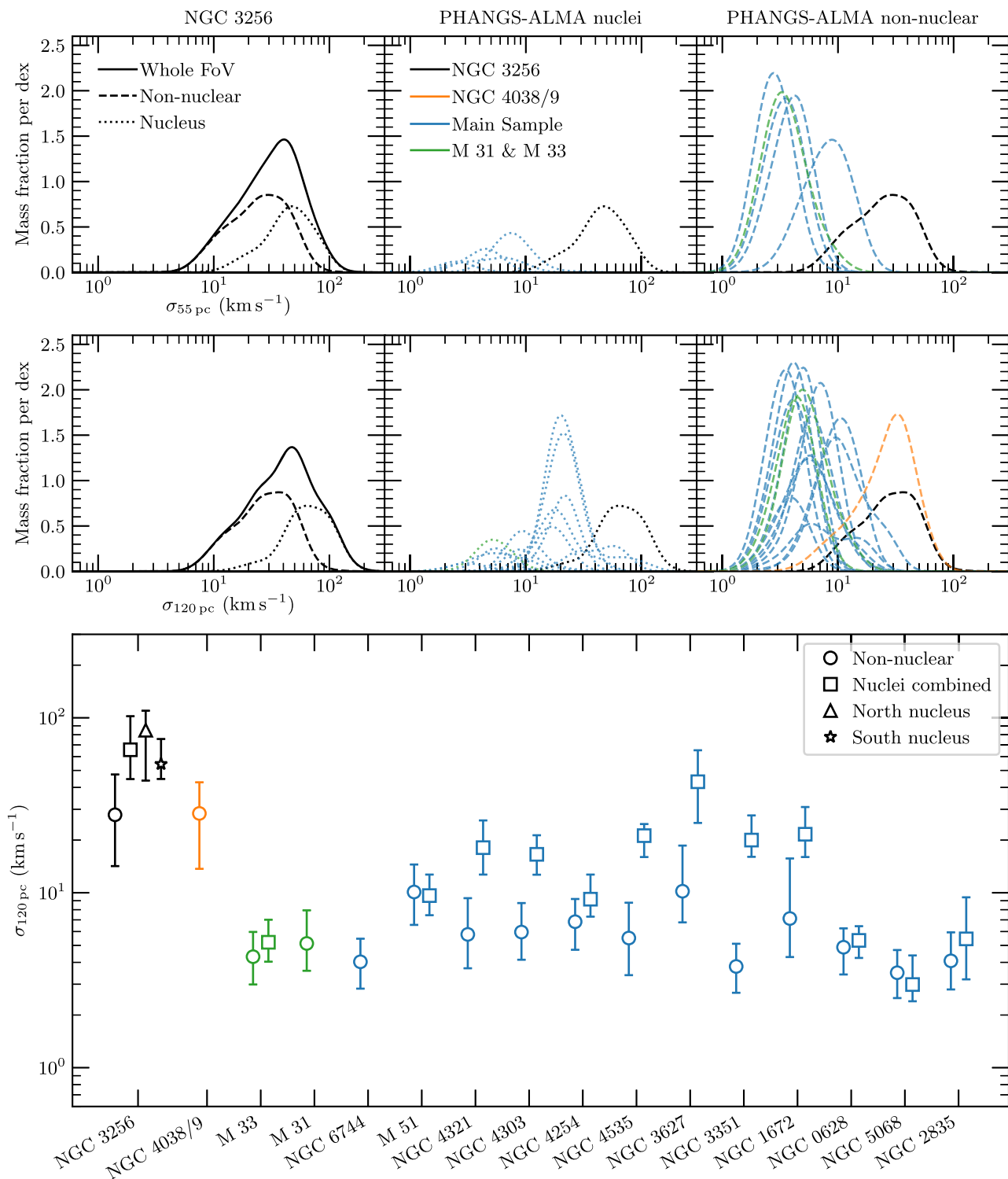
Figure 3. Same as Fig. 2, except for distributions of velocity dispersion measurements.

lution. The trend in the northern nucleus contains significant contamination from the outflow, driven by the northern nucleus, that becomes worse as the resolution is made coarser. This is due to improved surface brightness sensitivity at lower resolution increasing the detection of very wide spectral wings from the outflow. The high dispersion blobs in the 120 pc resolution map that are mostly absent in the 55 pc map are sightlines that are most affected by the outflow contribution.

Fig. 3 shows that the velocity dispersions for NGC 3256 are significantly higher than most of the PHANGS-ALMA sample. Almost no dispersions in the PHANGS-ALMA sample are as high as in the nuclei of NGC 3256, except for NGC 3627 discussed in Section 4.7.2. The nuclei of some PHANGS-ALMA galaxies overlap with the lower half of the NGC 3256 non-nuclear distribution.
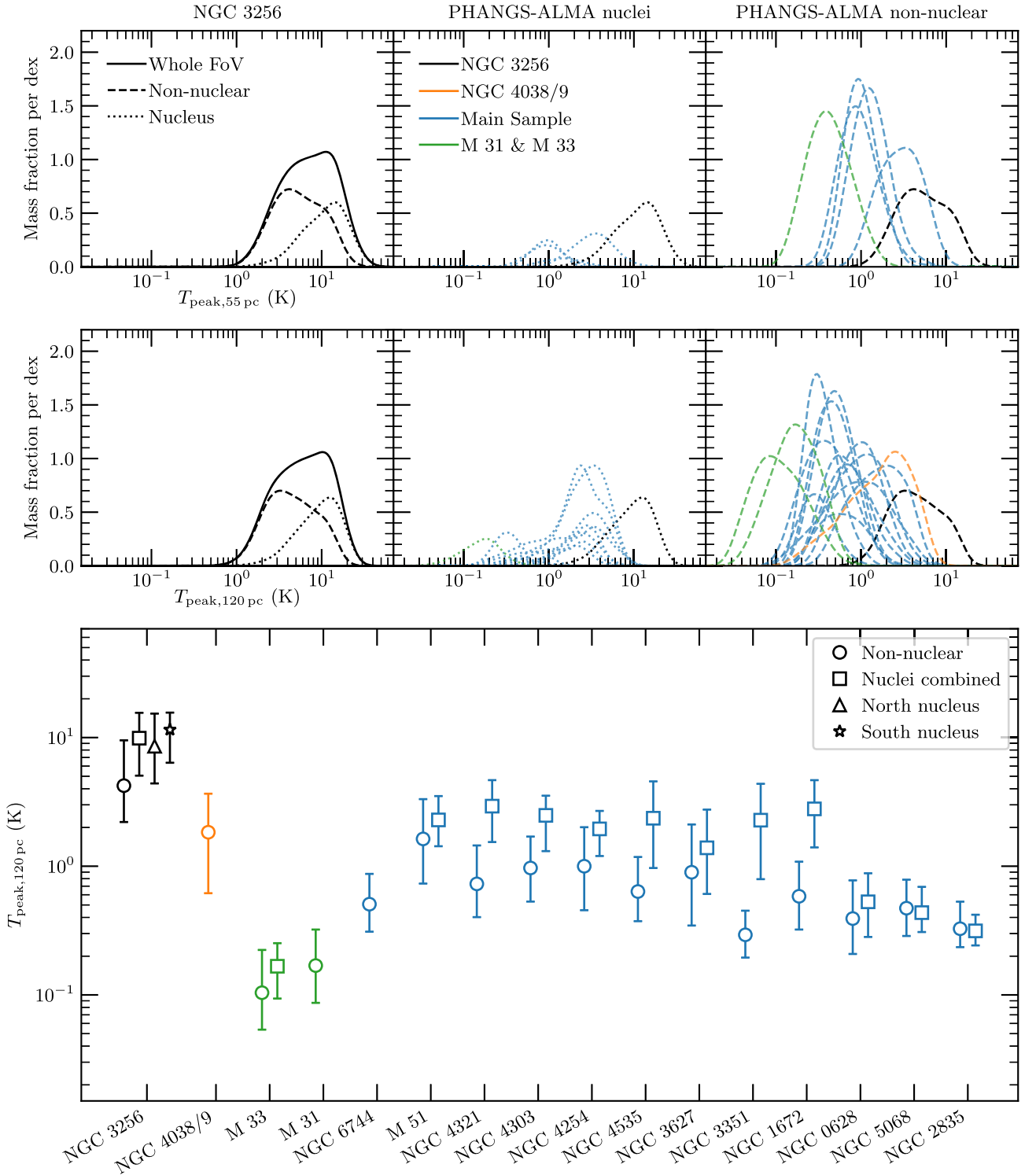
Figure 4. Same as Fig. 2, except for distributions of peak brightness temperature measurements.

4.3 Peak brightness temperature

The peak brightness temperature distributions from all pixels in NGC 3256 are centred near 7 K, range from 1 to 40 K, are slightly skewed to higher temperatures, and do not change significantly with resolution (see Fig. 4). The non-nuclear distribution peaks at ∼3 K and the combined nuclei distribution peaks at ∼15 K, but the inner 68 per cent of both distributions overlap significantly (3–11 K for the non-nuclear and 6–19 K for the nuclei).

While the nuclear and non-nuclear distributions in NGC 3256 overlap considerably, there is still a difference of about two in the median brightness temperatures between them. Assuming the sizes of molecular structures are not significantly different between those regions, this difference would indicate gas kinetic temperatures that are at most two times higher in the nuclei.

Similar to the velocity dispersions, the brightness temperatures in NGC 3256 reach higher values than all of the
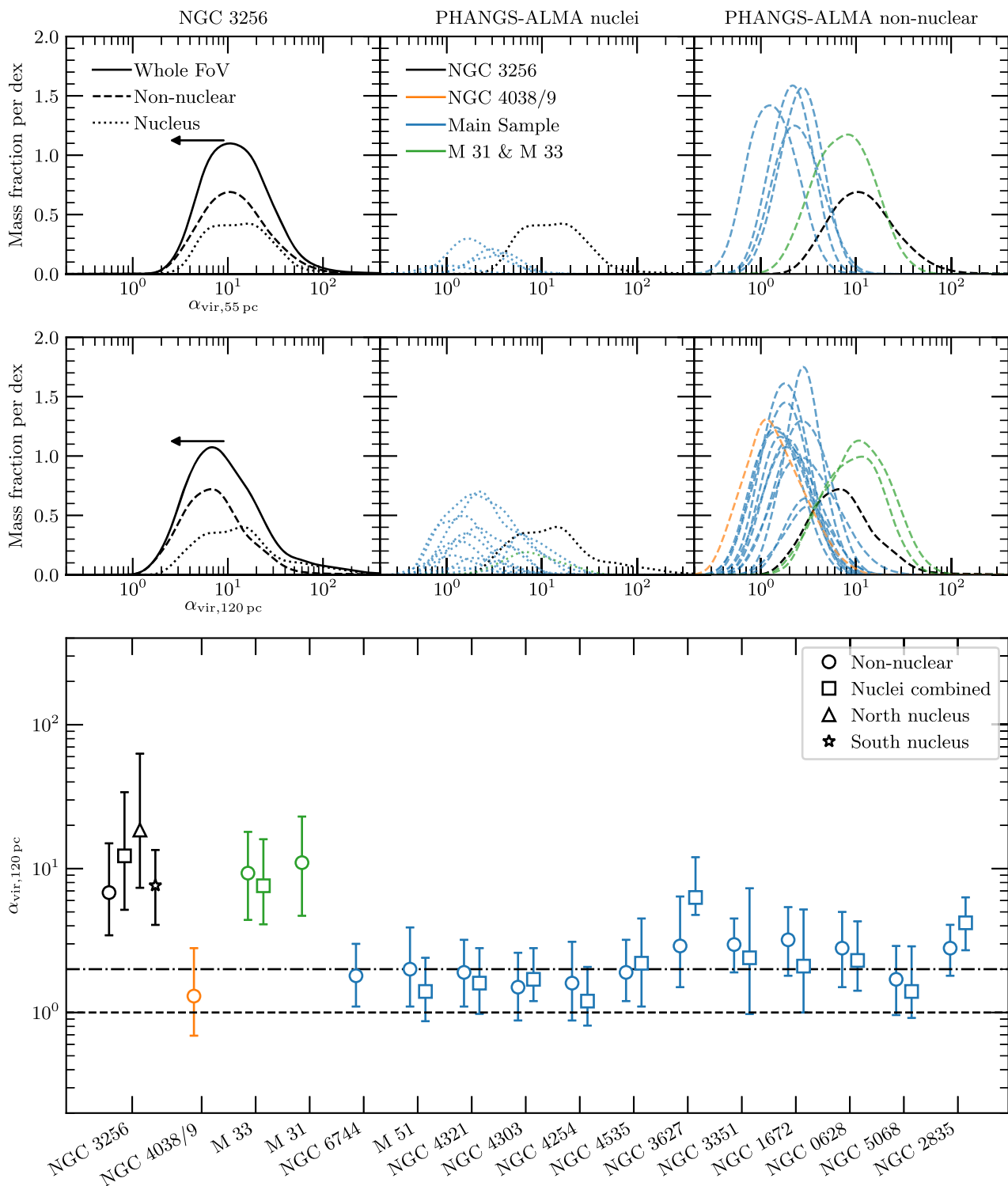
Figure 5. Same as Fig. 2, except for distributions of virial parameter measurements. The horizontal dashed line shows $\alpha_{\rm vir} = 1$ (virial equilibrium) and the dashed–dotted line shows $\alpha_{\rm vir} = 2$ (approximately bound or collapsing). The U/LIRG conversion factor of $1.38\,{\rm M}_\odot\,{\rm pc}^{-2}({\rm K\,km\,s}^{-1})^{-1}$ was used to calculate the surface densities for NGC 3256. Dividing the virial parameters of NGC 3256 by $\sim$4.5 would convert to the Galactic conversion factor of $6.25\,{\rm M}_\odot\,{\rm pc}^{-2}({\rm K\,km\,s}^{-1})^{-1}$ (used for all PHANGS-ALMA galaxies).

galaxies in the PHANGS-ALMA sample. Fig. 4 shows that most of the PHANGS-ALMA centres and the disc of M51 are consistent with only the non-nuclear distribution from NGC 3256.

4.4 Virial parameter

Fig. 5 shows the virial parameter distributions for all pixels in NGC 3256 peak around 10 but with long tails to near 1 and above 100. Changing the resolution slightly broadens the distributions when
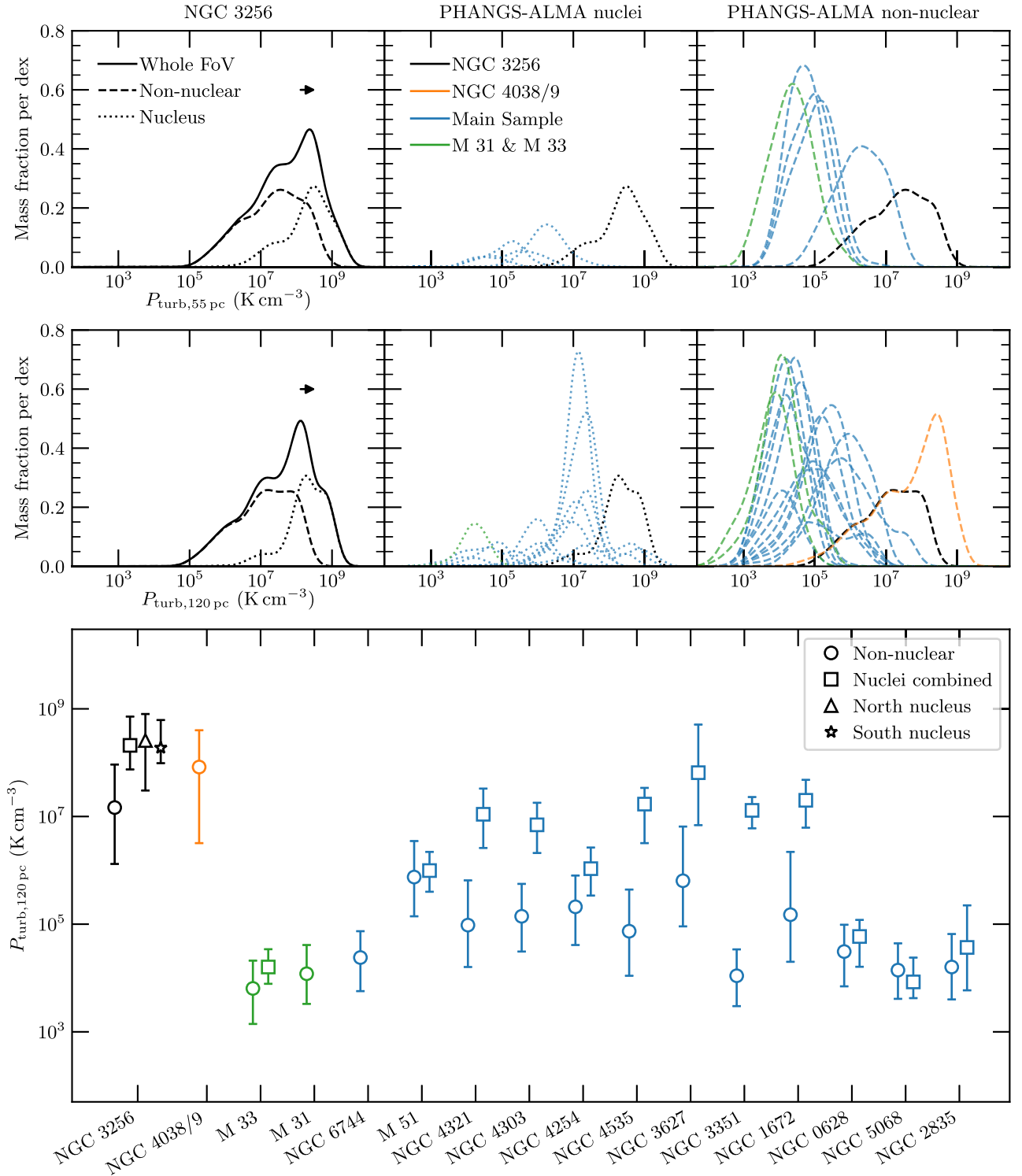
Figure 6. Same as Fig. 2, except for distributions of internal turbulent pressure measurements. The U/LIRG conversion factor of $1.38\,\mathrm{M_\odot\,pc^{-2}(K\,km\,s^{-1})^{-1}}$ was used to calculate the surface densities used here for NGC 3256. Multiplying the pressures by ~4.5 would convert to the Galactic conversion factor of $6.25\,\mathrm{M_\odot\,pc^{-2}(K\,km\,s^{-1})^{-1}}$ (used for all PHANGS-ALMA galaxies).

going from 55 to 120 pc. This occurs because at 55 pc the nuclear and non-nuclear distributions are very similar (except for more mass present in the non-nuclear pixels). At lower resolution, the non-nuclear pixels shift towards lower virial parameters, peaking around 6 at 120 pc, while the peak of the nuclear pixel distribution does not

move. Table 2 shows these changes are even more complex since the northern nucleus exhibits higher virial parameters at lower resolution but the southern nucleus shows the opposite trend. Non-nuclear virial parameters become slightly lower at lower resolution, but most of the mass has overlapping distributions between resolutions. In the

simple framework of balancing internal kinetic energy with self-gravity, the gas at these scales is not bound by gravity alone. It is worth highlighting here that changing from the U/LIRG to the Galactic conversion factor would result in the distributions being centred around two and would change the gas from being clearly unbound to marginally bound. Further analysis will have to wait for a better constrained CO conversion factor, possibly through a cloud decomposition of these data.

NGC 3256 appears quite different from most of the PHANGS-ALMA sample in virial parameter, as shown in Fig. 5. Most of the PHANGS-ALMA distributions hover around α_{vir} of about 1 or 2. Roughly half of the galaxies in the PHANGS-ALMA sample sit well below the distributions measured in NGC 3256. Interestingly, M31 and M33 are the most consistent with the distributions from NGC 3256 which may be due to properties unique to the ISM regime in those galaxies as well as observational effects (see sections 5.2.4 and 5.2.5 from Sun et al. 2018). A combination of reduced beam-filling factors at low surface densities, missing self-gravity from an underestimated CO conversion factor (also at low surface densities), and more dominant external pressures from larger fractions of atomic gas may be driving the higher virial parameters seen in M31 and M33.

4.5 Internal turbulent pressure

Internal turbulent pressure measured in all pixels exhibits the most complex distribution, with up to four peaks spanning a range from 10^5 to 10^{10} K cm^{-3} (see Fig. 6). It appears most of the mass at the highest pressures originates from the nuclear regions, and that the nuclear regions have almost a single narrowly peaked distribution around 5e8 K cm^{-3}. The additional nuclear component near 1e7 K cm^{-3} comes from pixels with surface densities below 1000 M$_\odot$ pc^{-2} (i.e. pixels not within the contours in Fig. 1) but that still lie within 1 kpc of the centre of the northern nucleus. While close to the northern nucleus in projection, these pixels have pressures consistent with the distribution from the non-nuclear pixels, indicating the gas properties are only at their most extreme very close to the centres of the nuclei. The southern nuclear region does not include such low pressures.

The comparison to the PHANGS-ALMA sample in Fig. 6 is quite similar to that for the velocity dispersion. The main difference is that the nuclear pressure distributions from NGC 3256 are not as extreme as the dispersions. This results in some of the PHANGS-ALMA main sample nuclei being consistent with the nuclei of NGC 3256. There is still a large fraction of discs and even whole galaxies from PHANGS-ALMA that have pressures 2–3 orders of magnitude lower than NGC 3256. The effect of the conversion factor choice is relatively small for the measured pressures given the width of the distributions. If the assumptions used to derive the turbulent pressure hold in NGC 3256 it contains some of the highest pressures in this sample of galaxies.

4.6 Two-dimensional view

2DGaussian KDEs of non-nuclear velocity dispersion versus surface density are shown in the top panel of Fig. 7. A bandwidth of 0.1 dex was used, and contours enclose 20, 50, and 80 per cent of the mass.

NGC 3256 is offset from the trend in the PHANGS-ALMA main sample and overlap region of NGC 4038/9. Most of this offset would be removed by switching NGC 3256 to the Galactic CO conversion factor. Fig. 7 makes it obvious that when using the U/LIRG conversion factor there is significant overlap in non-nuclear surface densities in NGC 3256 and the PHANGS-ALMA main sample. If the surface densities for NGC 3256 are correct then

the main driver pushing it off the PHANGS-ALMA trend is its high velocity dispersions.

The bottom panel of Fig. 7 shows the same 2D KDE but for NGC 3256 alone, at 55 pc resolution. Separate distributions for the non-nuclear, northern, and southern nucleus pixels are shown. The gap between peaks in the non-nuclear distribution is wider at higher resolution, driven mainly by a change in the surface densities. A similar bimodality is present in the northern nucleus, but the peaks are slightly shifted to higher surface densities than the non-nuclear peaks. The southern nucleus exhibits a unimodal distribution with its peak quite similar to the higher non-nuclear peak.

The bimodal distribution in the non-nuclear pixels appears to originate from measurements of truly non-nuclear pixels and some pixels that contain a contribution from the nuclear jet and/or outflow activity. Since the higher peak in the non-nuclear distribution is slightly closer to the peak in the southern nucleus distribution, it may be that the southern nucleus is the main contaminant to the non-nuclear pixels. This is reasonable since the jet from the southern nucleus may not be perfectly excluded from the non-nuclear pixels. It is also more likely the central 1 kpc boundary is not as accurate as for the northern nucleus due to the nearly edge-on orientation of the southern nucleus.

Bimodality in the northern nucleus distribution again points to the central gas structure being made up of a central region of high surface density with radius ∼250 pc surrounded by more non-nuclear-like gas from 250 pc outward.

4.7 Two detailed comparison studies

Here, we provide a more detailed comparison of two galaxies with NGC 3256, as they each present interesting cases. NGC 4038/9 is an important system for comparison because it is the only other merger analysed at the same resolution and in the same manner. It is the nearest merger at 22 Mpc (Schweizer et al. 2008) and contains ∼2 × 10^{10} M$_\odot$ in molecular gas (Gao et al. 2001). SFRs vary throughout the system, with the overlap region analysed by Sun et al. (2018, data originally presented by Whitmore et al. 2014) undergoing vigorous star formation (> 4 M$_\odot$ yr^{-1}, Brandl et al. 2009; Klaas et al. 2010; Bemis & Wilson 2019). Simulations place it at an intermediate merger stage, ∼40 Myr after its second pass (Karl et al. 2010). There does not appear to be any conclusive evidence of currently active nuclear outflows in the system.

We also examine NGC 3627 because it has extreme properties similar to NGC 3256 that often set it apart from the rest of the main PHANGS-ALMA sample. It is also a useful galaxy for comparison because it appears to follow the trends of extreme surface densities and dispersions relative to unbarred spiral galaxies shown by Sun et al. (2020b) in the full PHANGS-ALMA of 70 galaxies. It is at a distance of ∼11 Mpc (Lee & Jang 2013), is part of the Leo Triplet, shows evidence for LINER/Seyfert 2 nuclear activity (Peng et al. 1998), has a stellar mass of ∼10^{11} M$_\odot$ (Karachentsev & Kudrya 2014), and molecular gas mass of ∼10^{10} M$_\odot$ (Law et al. 2018). Optical images show a bar and two asymmetric spiral arms (Ptak et al. 2006) likely originating from interactions with NGC 3628 (Rots 1978; Soida et al. 2001). These morphological features also stand out in CO observations (Law et al. 2018; Sun et al. 2018). There is no evidence for currently active nuclear outflows in this system either.

4.7.1 NGC 4038/9

The surface density distribution of NGC 4038/9 is the only one to significantly exceed all measurements of surface densities from
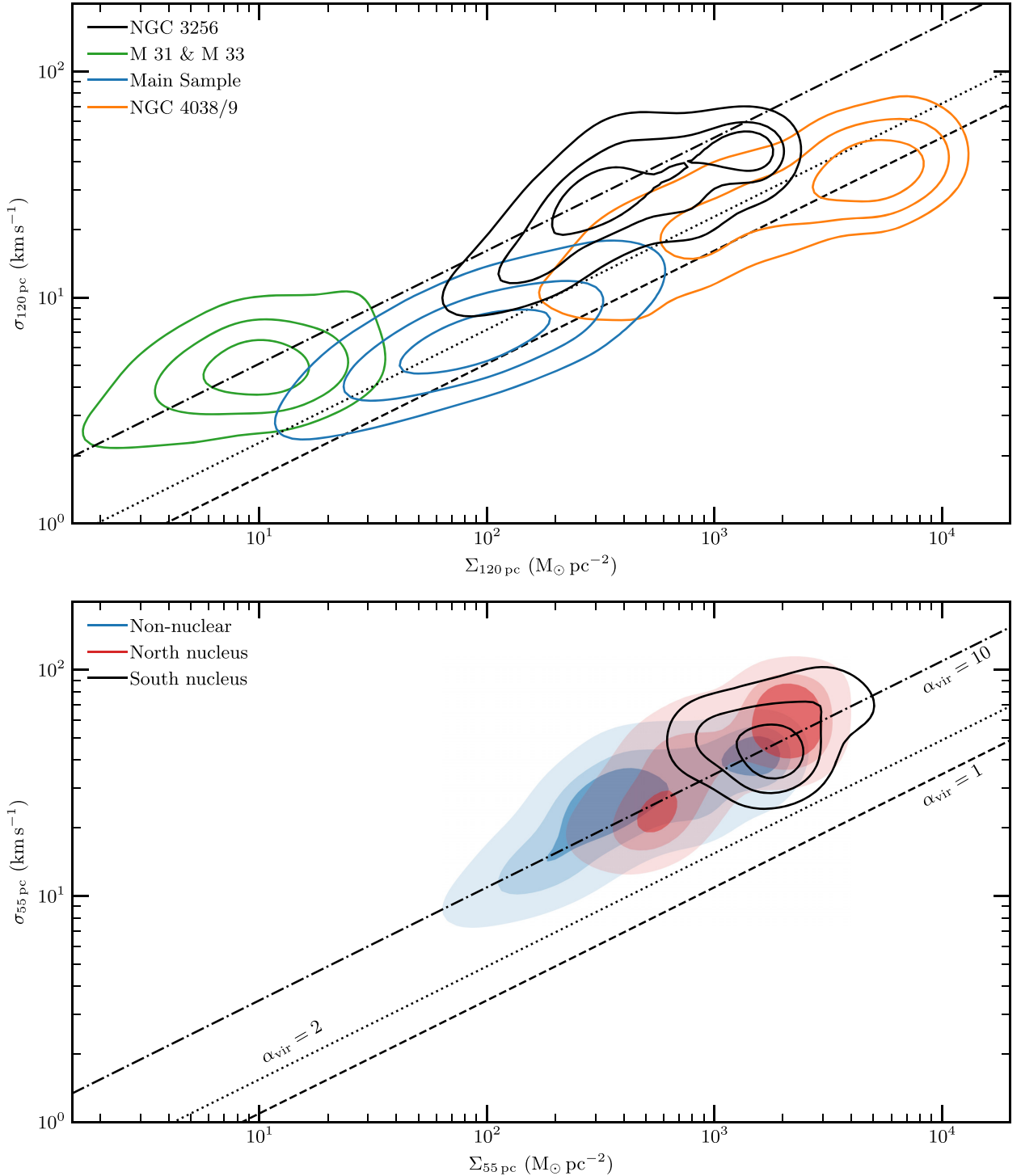
Figure 7. Velocity dispersion versus mass surface density with contours enclosing 20, 50, and 80 per cent of the total mass. Lines of constant virial parameter are shown to emphasize the difference in dynamical state between the PHANGS-ALMA main sample and NGC 3256. All PHANGS-ALMA galaxies use the Galactic CO conversion factor of $6.25\,M_\odot\,pc^{-2}(K\,km\,s^{-1})^{-1}$ while NGC 3256 uses the U/LIRG of $1.38\,M_\odot\,pc^{-2}(K\,km\,s^{-1})^{-1}$. Top: distributions from non-nuclear regions only, measured in 120 pc resolution maps. Bottom: all regions observed in NGC 3256 at 55 pc resolution.

NGC 3256, as shown in Fig. 2. About 50 per cent of the gas mass in the overlap region lies at surface densities above NGC 3256. Both the non-nuclear pixels and the nuclei of NGC 3256 are consistent with the lower half of the distribution from NGC 4038/9. About half the mass in the non-nuclear pixels of NGC 3256 lies at surface

densities below the NGC 4038/9 distribution. It is important to note that the Galactic conversion factor was used to calculate the mass surface densities for NGC 4038/9, as was done by Sun et al. (2018). In Section 5.5, we discuss the applicability of the Galactic conversion factor to the overlap region of NGC 4038/9, and how the comparison

to NGC 3256 changes if the U/LIRG conversion factor was used instead.

Fig. 3 shows that medians and widths of the velocity dispersion distributions in NGC 4038/9 and the non-nuclear pixels of NGC 3256 are very similar. The distributions also show similar shapes, with a sharper drop at high dispersions and a longer tail at low dispersions. However, the majority of mass in the nuclear pixels of NGC 3256 has velocity dispersions higher than the NGC 4038/9 distribution.

For peak brightness temperatures in Fig. 4, most of the gas measured in NGC 3256 is at higher values than NGC 4038/9. The lower half of the non-nuclear distribution in NGC 3256 overlaps with the upper half of the NGC 4038/9 distribution. Almost all of the mass in the nuclei of NGC 3256 has peak brightness temperatures above NGC 4038/9. This difference could be the result of higher molecular gas kinetic temperatures in NGC 3256 compared to the overlap region. It is reasonable to expect the gas to be warmer in NGC 3256 when its SFR surface densities range from 1.3 to 3.5 $M_\odot$ yr^{-1} kpc^{-2} on 512 pc scales in the non-nuclear regions (Wilson et al. 2019) compared to 0.21 to 0.84 $M_\odot$ yr^{-1} kpc^{-2} in the overlap region on kiloparsec scales (Bemis & Wilson 2019). Additionally, a $^{12}CO/^{13}CO$ $J=1$–0 ratio towards NGC 3256 of 35 (Aalto et al. 1991a) and of 13 towards the overlap region of NGC 4038/9 (Aalto et al. 1991b) may be indicative of higher gas temperatures in NGC 3256. However, while the difference in this line ratio likely indicates a difference in the gas properties of these two systems, additional transitions must be observed and modelled to determine if differing gas temperatures are truly present. For example, Zhu, Seaquist & Kuno (2003) included 2–1 and 3–2 ratios for some positions in the overlap region and still arrived at large velocity gradient solutions with temperatures of ∼30 or 120 K. The ratio can also be complicated by the different merger stages where late-stage mergers likely have more ^{12}CO produced via massive star formation processes (e.g. Sliwa et al. 2017; Brown & Wilson 2019).

The combination of higher surface densities but similar velocity dispersions results in virial parameters in NGC 4038/9 being significantly below all regions in NGC 3256 (see Fig. 5). NGC 4038/9 shows a very similar distribution to most of the galaxies in the PHANGS-ALMA main sample. This can be seen in Fig. 7 where NGC 4038/9 extends the trend seen in the discs of the main sample. The internal turbulent pressures calculated for NGC 4038/9 are consistent with all but the lowest portion of the NGC 3256 distributions, as shown in Fig. 6. Such similar internal pressures between the two mergers may be the result of similar driving mechanisms of turbulence, but their differing virial parameters appear to indicate dynamically important differences in the state of their gas density enhancements. Caveats related to the calculation of virial parameter and turbulent pressure, which also apply to NGC 4038/9, are discussed in Section 5.

4.7.2 NGC 3627

Fig. 2 shows that the disc of NGC 3627 has some of the highest surface densities among the PHANGS-ALMA main sample, only matched by M51 and the centre of NGC 4254. The upper half of the disc distribution overlaps with the non-nuclear and northern nucleus distribution of NGC 3256. The centre of NGC 3627 has the highest measured surface densities in the main sample, and even slightly exceeding the highest values from NGC 3256. Only the overlap region of NGC 4038/9 has higher surface densities. This is consistent with the comparison by Sun et al. (2020b) of the centres of 43 barred spiral galaxies having a ∼20 times higher mass-weighted median

surface density than pixels outside the central regions of 13 unbarred spiral galaxies. The centre of NGC 3627 also exhibits the broadest distribution of all of the centres from the main sample shown in Fig. 2 as well as the nuclei of NGC 3256. Only the distribution from the overlap region of NGC 4038/9 is wider.

Velocity dispersions in the disc of NGC 3627 lie above the majority of the measurements in the main sample in Fig. 3, but they only overlap with the lower ∼25 percent of the non-nuclear distribution from NGC 3256. However, the central distribution in NGC 3627 is consistent with both the upper half of the non-nuclear distribution and the lower half of the nuclei in NGC 3256. This is again consistent with the full PHANGS-ALMA sample, where Sun et al. (2020b) measure a ∼5 times higher mass-weighted velocity dispersion in their barred compared to unbarred galaxies, and again the width of the central distribution in NGC 3627 is one of the broadest compared to all centres from PHANGS-ALMA shown in Fig. 3.

Despite relatively wide distributions of peak brightness temperatures in NGC 3627 (see Fig. 4), both the disc and centre are consistent with most of the main sample. Brightness temperature distributions from NGC 3627 overlap with roughly the lower half of temperatures measured in the non-nuclear pixels of NGC 3256. The surface densities and velocity dispersions are similar to the mergers analysed here, and may be due to recent interactions with NGC 3628. However, the peak brightness temperatures of NGC 3627 are more in line with its relatively modest SFR of ∼5 $M_\odot$ yr^{-1} (Calzetti et al. 2015), or surface densities on about 300 pc scales reaching up to ∼0.3 $M_\odot$ yr^{-1} kpc^{-2} (Watanabe et al. 2011). Cormier et al. (2018) report $^{12}CO/^{13}CO$ $J=1$–0 ratios around 10 across NGC 3627, making it more similar to the overlap region in NGC 4038/9 than NGC 3256. This could be another case of kinetic temperatures being higher in NGC 3256, which is particularly interesting given how similar the other gas properties are between it and NGC 3627.

The centre of NGC 3627 stands out as having the highest virial parameters in the PHANGS-ALMA main sample in Fig. 5. It overlaps with the upper half of the non-nuclear distribution in NGC 3256, and is also consistent with both nuclei. The disc also exhibits quite high virial parameters for the main sample, overlapping with the non-nuclear and southern nucleus distributions from NGC 3256. This consistency is driven by the similar surface densities and velocity dispersions measured in NGC 3627 and NGC 3256. Fig. 6 shows similar results for the internal turbulent pressures. Sun et al. (2018) show the dispersions versus surface densities for just NGC 3627, split into disc and central regions, exhibiting a trend offset from the main sample like NGC 3256.

5 DISCUSSION

5.1 ISM structure

Sun et al. (2018) measure increasing median velocity dispersions with increasing beam FWHM (between 0.07 and 0.18 dex in the discs and 0.03 and 0.1 dex in the centres). This is indicative of the structured nature of the turbulent ISM because turbulent motions are expected to decrease at smaller scales (as in the size–linewidth relation; Larson 1981). A correlation between velocity dispersion and beam size is also measured in NGC 3256, but is very weak in all regions except the northern nucleus. The median dispersions in the non-nuclear region pixels increase by 0.05 dex, in the northern nucleus by 0.31 dex (see Section 4.2 for a discussion of how increased sensitivity to the nuclear outflow at lower resolution is likely the source of this trend), and in the southern nucleus by 0.04 dex. So despite more than a factor of two change in physical beam size,

there does not appear to be evidence for the turbulent size–linewidth relation at these scales.

Another signature of the structured ISM in the PHANGS-ALMA sample is in the decreasing median surface densities with increasing beam size (between 0.17 and 0.39 dex in the discs and 0.08 and 0.45 dex in the centres). This is caused by decreasing beam dilution as the resolution approaches the size of the clouds making up the ISM. In contrast, median surface densities in NGC 3256 only decrease by 0.02 and 0.01 dex, and not at all in the non-nuclear, northern, and southern nucleus, respectively. If the molecular gas is smooth across the physical scales analysed here, and star-forming overdensities primarily exist on scales smaller than 55 pc, then we would expect no trend in surface brightness with resolution.

We can also use our measurements of the peak brightness temperatures to probe the structure of the gas in NGC 3256. Given the optically thick nature of low-J transitions of CO, the brightness temperature approximately traces the kinetic temperature of the molecular gas. Taking the beam filling factor into account means the brightness temperature actually represents a lower limit for the kinetic temperature. If the emitting clouds are smaller than our 55 pc beam then the change in filling factor between 120 and 55 pc would be expected to result in a change of 0.68 dex, the ratio of beam areas. This scenario does not fit because we see only a 0.08 dex increase in the median brightness temperature in the 55 pc measurements compared to 120 pc.

If we assume the clouds are spherical we can instead solve for the diameter that would give the measured change in brightness temperature between 55 and 120 pc. Doing so we find the structures need to be ∼110 pc across. Since we should be able to resolve this size in our 55 pc map, this size is not consistent with the constant surface densities and dispersions measured as a function of beam size. This scenario would also not explain why the brightness temperature increases marginally between 80 and 55 pc and by roughly the same factor as between 120 and 80 pc.

The median temperature change can be explained if both the filling factor and the kinetic temperature of the gas are allowed to change between resolutions. However, if we assume the emitting sources are smaller than 55 pc and adopt the geometric change in the filling factor expected between our largest and smallest beam, then the kinetic temperatures would have to decrease by a factor of 4 as the beam FWHM decreases, which seems excessive.

One option not ruled out is that the bulk of the molecular gas is in a smooth medium that largely fills the volume but does not breakup into higher density clouds, even at 55 pc scales. In this scenario, the similarity of brightness temperature distributions across resolutions arises for the same reason we see no trend in surface density with resolution. So the lack of any strong trends with resolution in velocity dispersion, surface density, and brightness temperature indicates the molecular ISM in all regions observed in this merger has smoother structure than disc galaxies, at the same physical sizes.

5.2 Gas dynamics

Fig. 5 shows a significant difference in median virial parameters measured in NGC 3256 and the PHANGS-ALMA sample. Lines of constant virial parameter in Fig. 7 show how those differing virial parameters result in an offset between the two samples, potentially originating from a real difference in the dynamical states of the molecular gas.

The majority of gas across the PHANGS-ALMA galaxies is nearly self-gravitating or slightly overpressurized across almost 2 dex in surface density and 1 dex in velocity dispersion. The gas in NGC 3256

instead has enough excess velocity dispersion over about ∼1 dex in both surface density and dispersion that the gas appears to be nowhere near self-gravitating. However, both of these interpretations of the virial parameters do not include the contribution of external pressure confinement in estimating the boundedness of the gas in clouds.

Sun et al. (2020a) conclude that the contribution of external weight from atomic, stellar, and molecular mass in a clumpy ISM can balance the overpressurization seen in the PHANGS-ALMA sample and bring much of the gas into being bound in GMCs. Assuming the high virial parameters estimated in NGC 3256 are solely from the omission of external pressure, we can estimate the external mass surface densities required for pressure equilibrium within each beam. We find there would have to be between 65 and 4200 $M_\odot$ pc^{-2} in external mass confining the molecular clouds in the non-nuclear pixels of NGC 3256, and up to 10^4 $M_\odot$ pc^{-2} for some pixels in the nuclei. We summarize our method in Appendix A.

Stellar mass surface densities of nearby spirals can cover much of this mass range from ∼60 to 2000 $M_\odot$ pc^{-2} (Leroy et al. 2008; Jiménez-Donaire et al. 2019). Engargiola et al. (2003) measured ∼1e9 $M_\odot$ of atomic gas in the central 5 kpc of NGC 3256, giving an average atomic gas surface density of about 51 $M_\odot$ pc^{-2}. Including an estimate here for the contribution from large-scale and diffuse molecular gas external to the densest regions on GMC scales is not straightforward with an analysis like that of Sun et al. (2020a). However, from these estimates it seems plausible that a portion of the densest molecular gas we observe in NGC 3256 is being pressure confined by external matter. However, the highest dispersion gas likely does not have enough external pressure to be in pressure equilibrium with the surrounding material.

Estimates of pressures surrounding GMCs in systems like NGC 3256 have been made previously. H$\,$I cloud collisions have been estimated to produce localized pressures of ∼10^8 K cm^{-3} but result in average ambient pressures of only ∼5.5×10^5 K cm^{-3} (Jog & Solomon 1992). Wilson et al. (2003) estimate external pressures for supergiant molecular complexes in NGC 4038/9 due to the hot ISM to be on average 6×10^5 K cm^{-3}. They further argue that the low X-ray filling factor results in their pressure estimate being consistent with the localized pressure of Jog & Solomon (1992). Compared to NGC 3256, the localized pressures from Jog & Solomon (1992) exceed the non-nuclear pressures by an order of magnitude and are consistent with the pressures measured within the central 1 kpc of the nuclei. However, the ambient pressures in these models are too low by 2–3 orders of magnitude. Jog & Solomon (1992) explain that GMCs may be subject to the localized pressure if they are uniformly surrounded by and in direct contact with several H$\,$I clouds. Given the difference of up to an order of magnitude between the H$\,$I and molecular gas surface densities in NGC 3256, it is unlikely the atomic component is the dominant source of pressure confinement.

Johnson et al. (2015) estimated the external pressure on the Firecracker molecular cloud in NGC 4038/9 from the overlying molecular material to be ∼10^7 K cm^{-3}. Comparing this to the requisite external pressure of ∼10^9 K cm^{-3} needed to explain the velocity dispersion of the gas showed additional sources of pressure (like cloud–cloud collisions) were needed. Given the similar internal pressures but lower surface densities in NGC 3256 compared to NGC 4038/9, it is even less likely that external molecular gas could gravitationally bind the gas in NGC 3256. Tsuge et al. (2020a,b) estimated external pressures of ∼10^8 to 10^9 K cm^{-3} due to molecular cloud collisions for the five giant molecular complexes in NGC 4038/9. Similar external pressures could account for some of the highest internal pressures in NGC 3256, but would beg the question of whether there is enough molecular gas in the central
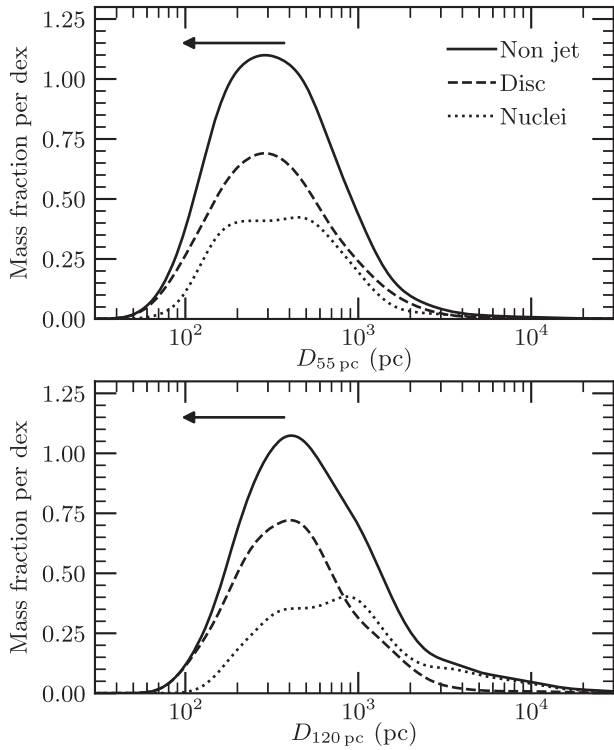
Figure 8. Cloud diameters calculated assuming a virial parameter of two for each pixel where surface density and velocity dispersion were measured in NGC 3256. Linestyles are the same as in Fig. 2. Arrows show how values would shift if we adopt the Milky Way CO conversion factor of $6.25\,M_\odot\,pc^{-2}(K\,km\,s^{-1})^{-1}$ instead of the LIRG conversion factor of $1.38\,M_\odot\,pc^{-2}(K\,km\,s^{-1})^{-1}$.

6 kpc of NGC 3256 undergoing cloud–cloud collisions to produce the pressures estimated here.

Returning to the offset of NGC 3256 relative to the PHANGS-ALMA sample in Fig. 7, NGC 3256 makes it clear that the velocity dispersion-surface density parameter space does not capture the full picture of the dynamics of molecular gas. The tight correlation seen across the PHANGS-ALMA main sample may be an artefact of selecting dynamically similar galaxies that are massive, disc-dominated, and star forming.

Related to this is the actual source of the turbulence. Krumholz et al. (2018) argue that the only way to power dispersions $\gtrsim 10\,km\,s^{-1}$ is through bulk gas flows that are ubiquitous in interacting galaxies. Differences in the power sources for turbulence between interacting and disc galaxies may be manifesting themselves in the state of the gas as probed by Fig. 7. It is not trivial to trace the sources of turbulence back from the gas dynamics in this way however since NGC 4038/9 lies along the PHANGS-ALMA main sample relation while NGC 3256 is offset from it. The individual properties of each interacting system may also change this offset, and the offset could change with time as the interactions evolve.

5.3 Virial diameter

Instead of asking if the gas is bound or not at the observed scales, we can ask at what size would the gas be in approximate free-fall collapse ($\alpha_{vir} = 2$), given the measured surface densities and velocity dispersions. Fig. 8 shows the Gaussian KDEs for these sizes. The all-pixel distributions peak around 300–400 pc between 55 and 120 pc resolution, respectively. Given the diameter at the peak of

the distributions is roughly five beams across at 55 pc resolution, a cloud-decomposition analysis would be able to identify if most of the gas is grouped into clouds of this size.

If this interpretation is correct then it would imply that the molecular gas is mostly gravitationally bound, but on quite large scales of a few hundred parsecs. One alternative could be that the velocity dispersions are biased towards high values by multiple clouds along the line of sight, and removing that effect would drive these sizes down. It is also possible that even at our highest resolution there are multiple clouds within the beam and that the cloud-to-cloud velocity differences are driving up the dispersion (and the sizes in Fig. 8). Without a good understanding of the cloud size and mass distributions in mergers like NGC 3256, this later alternative can only be explored with higher spatial resolution observations. Finally, it could be that the molecular gas is simply not bound at these scales and is behaving more similarly to the atomic gas traced by H I in spiral galaxies.

5.4 Expectations for a merger

High molecular gas surface densities, linked to enhanced quantities of molecular gas in interacting and merging galaxies, have been observed in many systems previously (e.g. Braine & Combes 1993; Kaneko et al. 2013; Violino et al. 2018). This has also been reproduced in numerical studies. Moreno et al. (2019), for example, measure a ∼18 per cent increase in cold-dense gas ($n = 10$–$1000\,cm^{-3}$) and a ∼240 per cent increase in cold ultradense gas ($n > 1000\,cm^{-3}$).

A possible origin of the extreme velocity dispersions in NGC 3256 is that the SFR was enhanced first, which then increased the velocity dispersion through stellar and supernova feedback. However, theoretical and numerical investigations into the sources of turbulent energy indicate that even at mass surface densities and turbulence levels replicating U/LIRG conditions and at the maximal limit of SFRs for discs, the gas velocity dispersion can only reach ∼10 km s^{-1} (Shetty & Ostriker 2012; Krumholz et al. 2018). Gas inflow was proposed by Krumholz et al. (2018) as the main mechanism to drive velocity dispersions above that limit. So while a portion of the measured velocity dispersion distribution can originate from star formation feedback, it is possible the highest dispersions are driven by gas flows.

Since the molecular gas at the scales observed in NGC 3256 appears smooth in comparison to disc galaxies and extreme external pressures are required to bind the gas, what are the actual sites of star formation like in this merger? It would seem that self-gravitating and collapsing overdensities must exist at scales smaller than 55 pc, potentially like Galactic clumps and cores. Moreno et al. (2019) report that interactions dramatically increase the mass fraction of the densest cold gas in their simulations, indicating the source of enhanced SFRs. However, this densest component only makes up ∼0.2 percent of the cold gas mass. Overall they measure an enhancement in diffuse molecular gas that cannot collapse. These models could imply that we are observing the high surface densities of the enhanced cold gas reservoir, but only at the scales where the gas is too diffuse to directly contribute to star formation. Marginally bound structures at the highest densities are driven to collapse by the interaction and thus the SFR increases, but the addition of turbulent energy from inflowing gas will act to overpressurize the bulk of the molecular gas.

5.5 Caveats

We first consider the applicability of using a CO conversion factor to estimate molecular gas masses from integrated CO line intensities.

Estimating mass from the optically thick CO emission with a conversion factor relies on the presence of virialized clouds which can relate their emitting surface area to the total mass in their volume. While the molecular gas in NGC 3256 is estimated to be well out of virial equilibrium due to self-gravity alone, it may be virialized when external pressure and gravitational terms (e.g. stars and the overall galactic potential) are included. If the molecular gas appears smooth on 55 pc scales because the majority of clouds are smaller than the beam, then the integrated line intensities would be proportional to the number of clouds within the beam. In lieu of optically thin emission, the collection of clouds within each beam may act optically thin such that each cloud contributes an average mass so the integrated intensity is still proportional to the total mass within the beam (the so-called mist model, Bolatto, Wolfire & Leroy 2013). Finally, beyond considering individual virialized clouds, the U/LIRG conversion factor used here has also been derived in the centres of U/LIRGs using CO spectra to estimate dynamical masses assuming smoothly distributed molecular gas (Downes & Solomon 1998).

The main assumption to be concerned with in the mist model when applying it to a system like NGC 3256 is that the sub-beam structure cannot be overlapping in spatial–spectral space. The high surface densities mean there is likely to be some degree of gas structures overlapping along the line of sight spatially, but the gas would also have to be Doppler shifted to the same velocities for the molecular mass to be underestimated. For this effect to entirely account for the offset in Fig. 7 would require ∼4.5 clouds both along the line of sight and at the same velocity in most pixels. An average of 4.5 clouds along each line of sight seems excessively large.

We now consider the value we chose for the conversion factor. Molecular gas properties potentially present in NGC 3256 such as higher temperatures, larger velocity dispersions, low CO optical depths, and non-virialized gas have all been argued as sources of low conversion factors in various studies of U/LIRGs (e.g. Wild et al. 1992; Papadopoulos & Seaquist 1999; Zhu et al. 2003). However, by switching to the Galactic value, the surface densities would increase by a factor of ∼4.5. This would result in the NGC 3256 non-nuclear sample overlapping considerably with the sample from NGC 4038/9, and it would also shift the bulk of the virial parameter distribution to ∼2. Gas at these densities and scales being bound by self-gravity would call into question the findings of Moreno et al. (2019) where they argue the majority of the enhanced molecular gas is not participating in star formation. It could instead be that the offset of NGC 3256 is real and that NGC 4038/9 would be better described by the U/LIRG conversion factor which would shift NGC 4038/9 closer to where NGC 3256 appears in Fig. 7. However, measurements of the conversion factor in NGC 4038/9 have actually come in either consistent with the Galactic value or even higher (Wilson et al. 2003; Schirm et al. 2014).

Differences in the proper conversion factor between NGC 3256 and NGC 4038/9 could originate from their differing merger stages as well as the regions analysed. Our observations of NGC 3256 cover the very centre of the system, where the conversion factor may be shifted to lower values (e.g. Weiß et al. 2001; Hitschfeld et al. 2008; Sliwa et al. 2013). It is also likely that the conversion factor varies significantly across different regions in this merger as Renaud et al. (2019) measure variations up to a factor of 2.2 in their simulation of an NGC 4038/9-like merger. They also expect spatial variations are even greater since they focused their analysis on actively star-forming regions. Directly estimating the conversion factor may be possible with these data but requires cloud decomposition in spatial and spectral dimensions. This will be investigated in a future paper.

Caution should be used when interpreting the velocity dispersions measured in both NGC 3256 and NGC 4038/9 due to the complex morphologies of interacting galaxies which makes it much more likely to observe multiple cloud structures along the line of sight. This is a limitation of the current pixel-based analysis. The degree to which both mergers, and even each region within the two systems, are affected by cloud multiplicity is likely to result in a non-trivial rearrangement of their distributions in Fig. 7. Our future cloud-decomposition analysis of NGC 3256 will help to eliminate this effect. We also note that while we attribute the spectral line widths to turbulence in our discussions, unresolved bulk motions also contribute to the measured dispersions. Given the high spatial resolution our observations however, an estimate of galactic rotation from the extrema of moment 1 maps contributes at most 5.5 km s^{-1} of dispersion across a single 120 pc beam. Bulk flow of gas from the merging process is also likely contributing in some regions of NGC 3256.

Interpretation of the virial parameters and internal turbulent pressures calculated for the mergers should also be made with caution. If the underlying assumptions are satisfied in NGC 3256 as well as in all of the galaxies presented by Sun et al. (2018), then using the same expressions for calculating these quantities should make the comparison of results straightforward. For the virial parameter, these assumptions include spherical clouds with density profiles of $\rho \propto r^{-2}$ that are the same size as the beam. The internal pressure relies on each beam being filled by one virialized cloud along each line of sight (Bertoldi & McKee 1992). Based on many previous studies of GMC properties in disc galaxies, these conditions are likely to hold in the main PHANGS-ALMA sample. However, without even higher resolution observations we cannot determine if these conditions hold in NGC 3256. The virial parameter distribution well above one indicates that the internal pressure would be underestimated, since the gas kinetic energy associated with bulk motions (like expansion) would not be accounted for in calculating the pressure. However, lines of sight with multiple components would overestimate the dispersion in the average cloud leading to an overestimation of the internal pressures.

6 CONCLUSIONS

We have observed the central 6 kpc of the closest LIRG, NGC 3256, in CO (2–1) with ALMA at GMC-scale resolution to obtain pixel-by-pixel distributions of mass surface density, velocity dispersion, peak brightness temperature, virial parameter, and internal turbulent pressure. From these distributions, we find:

(i) Assuming the U/LIRG conversion factor of 1.38 M$_\odot$ pc^{-2}(K km s^{-1})$^{-1}$, molecular mass surface densities range between 8 and 5500 M$_\odot$ pc^{-2}. This range is similar to the overlap region of NGC 4038/9, but extends to lower surface densities. NGC 3256 has surface densities above the majority of the disc measurements from PHANGS-ALMA reported by Sun et al. (2018).

(ii) Velocity dispersions range from 10 to 200 km s^{-1} in NGC 3256. The median outside the central kiloparsec radius is 25 km s^{-1}. These velocity dispersions are well above the majority of the PHANGS-ALMA disc galaxies, and are consistent with NGC 4038/9.

(iii) The vast majority of the gas appears unbound at 55 pc scales with virial parameters above 3, and medians even reaching 7–19. Coupled to this, we estimate very high turbulent pressures from 10^5 to 10^{10} K cm^{-3}. External pressure on GMCs may bind a fraction of

the gas, but there is still likely a significant fraction of mass that is unbound.

(iv) 50 per cent of the mass in the non-nuclear pixels of NGC 3256 has peak brightness temperatures significantly above almost all measurements in the main PHANGS-ALMA sample as well as the overlap region of NGC 4038/9. All measurements in the nuclei of NGC 3256 are above those in all other galaxies analysed here. This suggests the majority of molecular gas in NGC 3256 is significantly warmer than disc galaxies and even the most vigorously star forming region of NGC 4038/9.

(v) The observation of little or no trend in surface density, velocity dispersion, and peak brightness temperature with resolution indicates the molecular medium has a smoother structure at 55 pc scales than in the PHANGS-ALMA disc galaxies. A smooth molecular ISM appearing unbound on these scales could be consistent with FIRE-2 (Feedback In Realistic Environments-2) numerical results (Moreno et al. 2019). It may also be that gas at these scales in NGC 3256 more closely resembles the dynamics of giant molecular associations in disc galaxies.

An additional test of the boundedness of the gas in NGC 3256 will be carried out using a spatial and spectral decomposition of the CO emission in a future paper. Instead of assuming the beam size represents the relevant scale, this analysis will produce empirical estimates of the sizes of the molecular structures. We will also attempt to estimate the CO conversion factor from the cloud size and linewidth catalog. However, the virial parameter estimates reported in this work make it likely that this approach will produce at best an upper limit. Independent methods to estimate the conversion factor (e.g. estimating dust masses from the continuum or optically thin molecular line isotopologues) should also be investigated.

Applying both pixel-by-pixel and cloud-decomposition analyses to more merger systems at this resolution will help to determine if the apparent ISM dynamics and structure in NGC 3256 are general properties of these extreme systems. It can also further test the universality of gas dynamical state reported by Sun et al. (2018) across the PHANGS-ALMA main sample and overlap region in NGC 4038/9. In a forthcoming paper, we will apply these analyses, at the same physical scales, to the entire NGC 4038/9 merger system in CO (2–1). This will also allow us to probe the nuclear regions for similarities with the nuclei of other galaxies.

Finally, higher resolution imaging of NGC 3256 in CO (2–1) would explore at what scale the molecular gas goes from a smooth medium to the clumpy one we assume must exist due to the presence of significant star formation. ALMA can observe down to ≈ 9 pc scales to search for significant changes in the physical quantities discussed here. Any trends with resolution would indicate a structured ISM like what is seen in the PHANGS-ALMA galaxies at 45 pc. Whether we will find clouds on scales smaller than 55 pc in NGC 3256 that are analogous to GMCs in nearby discs, or that the molecular gas remains unbound down to scales and densities that are more similar to Galactic clumps or cores is a question that awaits maximal resolution data from ALMA.

ACKNOWLEDGEMENTS

DATA AVAILABILITY

This paper makes use of the following ALMA data: ADS/JAO.ALMA#2015.1.00714.S (accessed from the ALMA Science portal at almascience.org). ALMA is a partnership of ESO (representing its member states), NSF (USA), and NINS (Japan), together with NRC (Canada), MOST, and ASIAA (Taiwan), and KASI (Republic of Korea), in cooperation with the Republic of Chile. The Joint ALMA Observatory is operated by ESO, AUI/NRAO, and NAOJ. The National Radio Astronomy Observatory is a facility of the National Science Foundation operated under cooperative agreement by Associated Universities, Inc.

The derived data generated in this research will be shared on reasonable request to the corresponding author.

REFERENCES

Aalto S., Black J. H., Booth R. S., Johansson L. E. B., 1991a, A&A, 247, 291
Aalto S., Black J. H., Johansson L. E. B., Booth R. S., 1991b, A&A, 249, 323
Aalto S., Booth R. S., Black J. H., Johansson L. E. B., 1995, A&A, 300, 369
Astropy Collaboration et al., 2013, A&A, 558, A33
Astropy Collaboration et al., 2018, AJ, 156, 123
Bemis A., Wilson C. D., 2019, AJ, 157, 131
Bertoldi F., McKee C. F., 1992, ApJ, 395, 140
Blitz L., Thaddeus P., 1980, ApJ, 241, 676
Bolatto A. D., Leroy A. K., Rosolowsky E., Walter F., Blitz L., 2008, ApJ, 686, 948
Bolatto A. D., Wolfire M., Leroy A. K., 2013, ARA&A, 51, 207
Booth C. M., Agertz O., Kravtsov A. V., Gnedin N. Y., 2013, ApJ, 777, L16
Braine J., Combes F., 1993, A&A, 269, 7
Brandl B. R. et al., 2009, ApJ, 699, 1982
Brown T., Wilson C. D., 2019, ApJ, 879, 17
Calzetti D. et al., 2015, AJ, 149, 51
Catinella B. et al., 2018, MNRAS, 476, 875
Colombo D. et al., 2014, ApJ, 784, 3
Cormier D. et al., 2018, MNRAS, 475, 3909
Dale J. E., Bonnell I. A., 2008, MNRAS, 391, 2
Dame T. M. et al., 1987, ApJ, 322, 706
Downes D., Solomon P. M., 1998, ApJ, 507, 615
Engargiola G., Plambeck R. L., Rosolowsky E., Blitz L., 2003, ApJS, 149, 343
Farrah D. et al., 2001, MNRAS, 326, 1333
Federrath C., Klessen R. S., 2012, ApJ, 761, 156
Field G. B., Blackman E. G., Keto E. R., 2011, MNRAS, 416, 710

Fukui Y. et al., 1999, PASJ, 51, 745

Gao Y., Lo K. Y., Lee S. W., Lee T. H., 2001, ApJ, 548, 172

Genzel R., Stutzki J., 1989, ARA&A, 27, 41

Ginsburg A. et al. , 2019, radio-astro-tools/spectral-cube: v0.4.4, Available at: https://zenodo.org/record/2573901#.X73o880zbIU

Girichidis P. et al., 2016, ApJ, 816, L19

Harada N., Sakamoto K., Martín S., Aalto S., Aladro R., Sliwa K., 2018, ApJ, 855, 49

He H., Wilson C. D., Sliwa K., Iono D., Saito T., 2020, MNRAS, 496, 5243

Heyer M. H., Carpenter J. M., Snell R. L., 2001, ApJ, 551, 852

Heyer M., Krawczyk C., Duval J., Jackson J. M., 2009, ApJ, 699, 1092

Hitschfeld M. et al., 2008, A&A, 479, 75

Howard C. S., Pudritz R. E., Harris W. E., 2017, MNRAS, 470, 3346

Howell J. H. et al., 2010, ApJ, 715, 572

Hunter J. D., 2007, Comput. Sci. Eng., 9, 90

Iono D., Yun M. S., Mihos J. C., 2004, ApJ, 616, 199

Jiménez-Donaire M. J. et al., 2019, ApJ, 880, 127

Jog C. J., Solomon P. M., 1992, ApJ, 387, 152

Johnson K. E., Leroy A. K., Indebetouw R., Brogan C. L., Whitmore B. C., Hibbard J., Sheth K., Evans A. S., 2015, ApJ, 806, 35

Kaneko H., Kuno N., Iono D., Tamura Y., Tosaki T., Nakanishi K., Sawada T., 2013, PASJ, 65, 20

Karachentsev I. D., Kudrya Y. N., 2014, AJ, 148, 50

Karl S. J., Naab T., Johansson P. H., Kotarba H., Boily C. M., Renaud F., Theis C., 2010, ApJ, 715, L88

Keller B. W., Kruijssen J. M. D., Wadsley J. W., 2020, MNRAS, 493, 2149

Keto E. R., Myers P. C., 1986, ApJ, 304, 466

Klaas U., Nielbock M., Haas M., Krause O., Schreiber J., 2010, A&A, 518, L44

Klassen M., Pudritz R. E., Peters T., 2012, MNRAS, 421, 2861

Kluyver T. et al., 2016, in Loizides F., Schmidt B., eds, 20th International Conference on Electronic Publishing, Positioning and Power in Academic Publishing: Players, Agents and Agendas. IOS Press, Netherlands, p. 87

Krumholz M. R., Dekel A., McKee C. F., 2012, ApJ, 745, 69

Krumholz M. R., Burkhart B., Forbes J. C., Crocker R. M., 2018, MNRAS, 477, 2716

Larson R. B., 1981, MNRAS, 194, 809

Law C. J., Zhang Q., Ricci L., Petitpas G., Jiménez-Donaire M. J., Ueda J., Lu X., Dunham M. M., 2018, ApJ, 865, 17

Lee M. G., Jang I. S., 2013, ApJ, 773, 13

Leroy A., Bolatto A., Walter F., Blitz L., 2006, ApJ, 643, 825

Leroy A. K., Walter F., Brinks E., Bigiel F., de Blok W. J. G., Madore B., Thornley M. D., 2008, AJ, 136, 2782

Leroy A. K. et al., 2015, ApJ, 801, 25

Leroy A. K. et al., 2016, ApJ, 831, 16

McKee C. F., Zweibel E. G., 1992, ApJ, 399, 551

McMullin J. P., Waters B., Schiebel D., Young W., Golap K., 2007, in Shaw R. A., Hill F., Bell D. J., eds, ASP Conf. Ser. Vol. 376, Astronomical Data Analysis Software and Systems XVI. Astron. Soc. Pac., San Francisco, p. 127

Michiyama T. et al., 2018, ApJ, 868, 95

Mihos J. C., Hernquist L., 1996, ApJ, 464, 641

Mizuno A., Onishi T., Yonekura Y., Nagahama T., Ogawa H., Fukui Y., 1995, ApJ, 445, L161

Mizuno N., Rubio M., Mizuno A., Yamaguchi R., Onishi T., Fukui Y., 2001, PASJ, 53, L45

Moreno J. et al., 2019, MNRAS, 485, 1320

Noguchi M., 1988, A&A, 203, 259

Ochsenbein F., Bauer P., Marcout J., 2000, A&AS, 143, 23

Ohyama Y., Terashima Y., Sakamoto K., 2015, ApJ, 805, 162

Padoan P., Haugbølle T., Nordlund, Å., Frimann S., 2017, ApJ, 840, 48

Papadopoulos P. P., Seaquist E. R., 1999, ApJ, 516, 114

Papadopoulos P. P., van der Werf P. P., Xilouris E. M., Isaak K. G., Gao Y., Mühle S., 2012, MNRAS, 426, 2601

Pedregosa F. et al., 2011, J. Mach. Learn. Res., 12, 2825

Peng C. Y., Ho L. C., Filippenko A. V., Sargent W. L. W., 1998, in American Astronomical Society Meeting Abstracts. p. 06.07

Ptak A., Colbert E., van der Marel R. P., Roye E., Heckman T., Towne B., 2006, ApJS, 166, 154

Renaud F., Bournaud F., Agertz O., Kraljic K., Schinnerer E., Bolatto A., Daddi E., Hughes A., 2019, A&A, 625, A65

Rosolowsky E., 2007, ApJ, 654, 240

Rosolowsky E., Blitz L., 2005, ApJ, 623, 826

Rots A. H., 1978, AJ, 83, 219

Saintonge A. et al., 2017, ApJS, 233, 22

Saito T. et al., 2017, ApJ, 835, 174

Sakamoto K., Aalto S., Combes F., Evans A., Peck A., 2014, ApJ, 797, 90

Sanders D. B., Mirabel I. F., 1996, ARA&A, 34, 749

Sanders D. B., Mazzarella J. M., Kim D. C., Surace J. A., Soifer B. T., 2003, AJ, 126, 1607

Sargent M. T. et al., 2014, ApJ, 793, 19

Schirm M. R. P. et al., 2014, ApJ, 781, 101

Schweizer F. et al., 2008, AJ, 136, 1482

Seabold S., Perktold J., 2010, in van der Walt S., Millman J., eds, Python in Science Conf. Ser., Available at: http://conference.scipy.org/proceedings/scipy2010/

Shetty R., Ostriker E. C., 2012, ApJ, 754, 2

Sliwa K. et al., 2013, ApJ, 777, 126

Sliwa K., Wilson C. D., Aalto S., Privon G. C., 2017, ApJ, 840, L11

Soida M., Urbanik M., Beck R., Wielebinski R., Balkowski C., 2001, A&A, 378, 40

Solomon P. M., Rivolo A. R., Barrett J., Yahil A., 1987, ApJ, 319, 730

Stierwalt S. et al., 2013, ApJS, 206, 1

Sun J. et al., 2018, ApJ, 860, 172

Sun J. et al., 2020a, ApJ, 892, 148

Sun J. et al., 2020b, ApJ, 901, L8

Tsuge K., Fukui Y., Tachihara K., Sano H., Tokuda K., Ueda J., Iono D., Finn M. K., 2020a, PASJ, preprint (arXiv:1909.05240)

Tsuge K., Tachihara K., Fukui Y., Sano H., Tokuda K., Ueda J., Iono D., 2020b, preprint (arXiv:2005.04075)

Utomo D., Blitz L., Davis T., Rosolowsky E., Bureau M., Cappellari M., Sarzi M., 2015, ApJ, 803, 16

Utomo D. et al., 2018, ApJ, 861, L18

van der Walt S., Colbert S. C., Varoquaux G., 2011, Comput. Sci. Eng., 13, 22

Veilleux S., Kim D. C., Sanders D. B., 2002, ApJS, 143, 315

Violino G., Ellison S. L., Sargent M., Coppin K. E. K., Scudder J. M., Mendel T. J., Saintonge A., 2018, MNRAS, 476, 2591

Watanabe Y., Sorai K., Kuno N., Habe A., 2011, MNRAS, 411, 1409

Weiß A., Neininger N., Hüttemeister S., Klein U., 2001, A&A, 365, 571

Wenger M. et al., 2000, A&AS, 143, 9

Whitmore B. C. et al., 2014, ApJ, 795, 156

Wild W., Harris A. I., Eckart A., Genzel R., Graf U. U., Jackson J. M., Russell A. P. G., Stutzki J., 1992, A&A, 265, 447

Wilson C. D., Scoville N., 1990, ApJ, 363, 435

Wilson C. D., Scoville N., Madden S. C., Charmandaris V., 2003, ApJ, 599, 1049

Wilson C. D., Elmegreen B. G., Bemis A., Brunetti N., 2019, ApJ, 882, 5

Wong T. et al., 2011, ApJS, 197, 16

Zhu M., Seaquist E. R., Kuno N., 2003, ApJ, 588, 243

APPENDIX A: ESTIMATING REQUIRED EXTERNAL MATERIAL

The virial parameters presented in Section 4.4 neglect the effect of external pressure on the cloud. We make a rough estimate of the pressure required to balance the internal turbulent pressure following a simplified form of that by Sun et al. (2020a). We aim to satisfy the criterion that the external pressure, P_{ext}, is equal to the internal pressure, P_{turb}. A simple expression for the gravitational pressure from mass external to the cloud is

$$P_{ext} k_B = C G \Sigma_{cloud} \Sigma_{tot} \tag{A1}$$

where k_B is the Boltzmann constant, C is a constant that contains normalizations for the assumed geometries of all of the material, G is the gravitational constant, Σ_{cloud} is the mass surface density of the molecular cloud, and Σ_{tot} is the surface density of all material along the line of sight.

Neglecting dark matter in the inner portion of this merger, Σ_{tot} is made up of

$$\Sigma_{\text{tot}} = \Sigma_{\text{cloud}} + \Sigma_{\text{ext,mol}} + \Sigma_\star + \Sigma_{\text{atom}} \tag{A2}$$

$$= \Sigma_{\text{cloud}} + \Sigma_{\text{ext}} \tag{A3}$$

where $\Sigma_{\text{ext, mol}}$ is the molecular gas surface density outside the cloud, $\Sigma_\star$ is the stellar surface density, Σ_{atom} is the atomic surface density, and Σ_{ext} is the sum of the components external to the cloud. Rewriting the external pressure with these separate terms gives

$$P_{\text{ext}} k_B = G \Sigma_{\text{cloud}} \left(C_1 \Sigma_{\text{cloud}} + C_2 \Sigma_{\text{ext}} \right) \tag{A4}$$

where $C_1 \Sigma_{\text{cloud}}$ accounts for the self-gravity of the cloud and $C_2 \Sigma_{\text{ext}}$ the weight of material external to the cloud. C_1 and C_2 are again constants that depend on the geometry of these components. Assuming constant density within a spherical cloud, $C_1 = 3\pi/8$ (e.g. equation A2 from Sun et al. 2020a).

Setting the external pressure equal to the measured internal pressure and rearranging equation (A4) we have an expression for the external mass surface density required to balance the internal turbulent pressure

$$\Sigma_{\text{ext}} = \frac{1}{C_2} \left(\frac{k_B P_{\text{turb}}}{G \Sigma_{\text{cloud}}} - \frac{3\pi}{8} \Sigma_{\text{cloud}} \right). \tag{A5}$$

If we treat C_2 as tunable between $3\pi/8$ (spherical) and $\pi/2$ (disc with scale height much greater than the molecular disc scale height), then we can explore a reasonable range of external pressures given different combinations of relative geometries of the multiple components. This was the most useful approach considering that C_2 must encode the volumetric average of all three external components relative to the molecular clouds in a morphologically disturbed merger.

Calculating external surface densities, pixel-by-pixel using our measurements at 55 pc resolution, gives disc mass-weighted 16, 50, and 84 percentiles of $(100, 1000, \text{ and } 3000\,\text{M}_\odot\,\text{pc}^{-2})/C_2$. The combined-nuclei percentiles are $(2 \times 10^3,\ 6 \times 10^3,\ \text{and}\ 20 \times 10^3\,\text{M}_\odot\,\text{pc}^{-2})/C_2$. The same calculation for the PHANGS-ALMA sample results in most pixels having external surface densities of zero or less, which we interpret as the majority of gas being self-gravity dominated (Sun et al. 2020a). The remaining pixels in the PHANGS-ALMA sample appear around $(50 - 100\,\text{M}_\odot\,\text{pc}^{-2})/C_2$.

An important component this model neglects is the pressure contribution from self-gravity of the external material (e.g. the atomic term in equation A9 from Sun et al. 2020a). This primarily depends on the surface density of the atomic gas, and acts to reduce the external surface density required to confine the molecular cloud. Galaxies in the PHANGS-ALMA sample are strongly impacted by this term, and so the full treatment by Sun et al. (2020a) is recommended to assess their pressure equilibrium. We do not expect the atomic surface density to provide a very substantial correction in a merger. Since we estimate NGC 3256 requires significantly higher external surface densities than the PHANGS-ALMA galaxies, it is unlikely the missing external self-gravity term would drastically alter our results.

This paper has been typeset from a TEX/LATEX file prepared by the author.